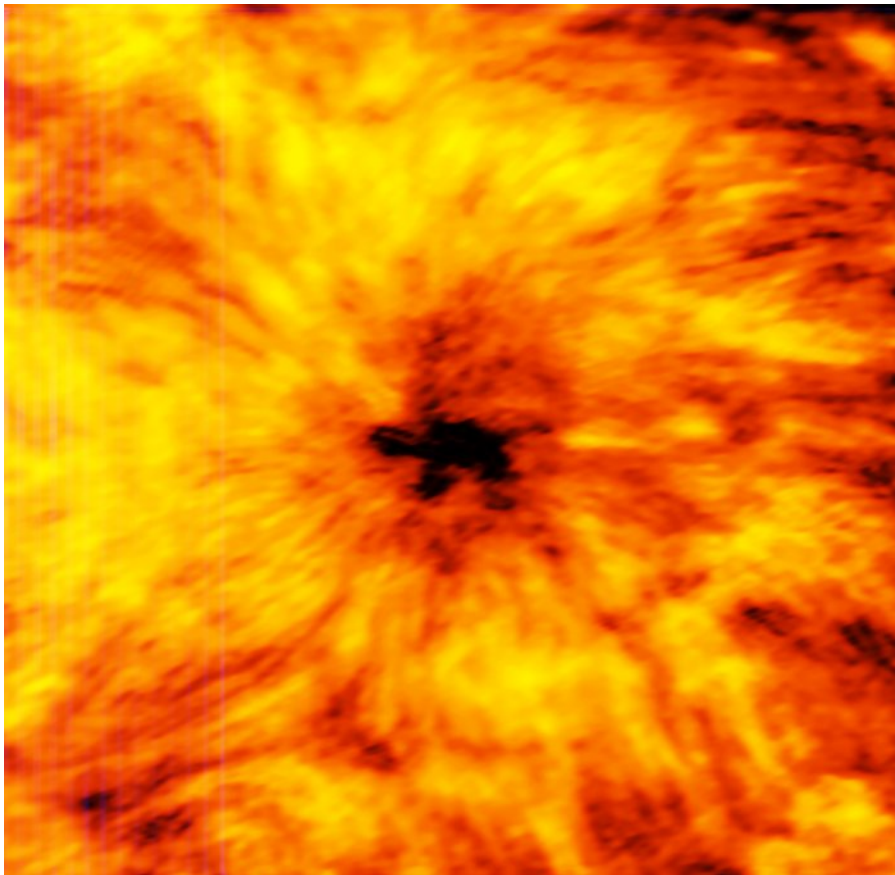


ESO Development Plan Study: Solar Research with ALMA Final Report

R. Brajša, I. Skokić, M. Bárta,
T. Bastian, M. Shimojo, S. White, K. Iwai

2017-05-26



Sunspot observed by ALMA in Band 6

TABLE OF CONTENTS

1	Introduction	3
1.1	Purpose	3
1.2	Scope	3
1.3	Related Documents	3
1.4	Accomplishments	3
1.5	Acknowledgments	4
2	Solar Observing Modes	6
2.1	Solar Filters	6
2.2	Mixer Detuning	7
2.3	Linearity of the MD Modes	8
2.4	IF Attenuator Settings	10
2.5	Water Vapor Radiometers	10
2.6	Choice of Frequencies	11
2.7	Spatial Scales	11
2.8	Calibrator Selection	12
2.9	Time and Scheduling Constraints	13
2.10	Joint Observations	15
3	Interferometric Solar Observing	16
3.1	Validation of Interferometric Observations	16
3.2	Phase Calibration Transfer	19
3.3	Bandpass Calibration	20
3.4	Amplitude Calibration	21
3.5	Solar Observing Sequence	25
3.6	Mosaicking	25
3.7	Data and Image Synthesis	26
3.8	Noise Level of Solar Images	28
3.9	Imaging Artifacts Above the Solar Limb	30
3.10	Co-alignment between ALMA and other instruments	31
4	Single-dish solar observing	34
4.1	Fast-scan Mapping	34
4.1.1	Lissajous Mapping	35
4.1.2	Double-circle Fast-scanning	36
4.2	Calibration Strategy	38
4.3	Examples of Single-dish Images	45
5	Software requirements for solar observing	50
5.1	ALMA Observing Tool	50
5.2	Coordinate Conversions for Solar Observing	50
5.3	ALMA Solar Ephemeris Generator Tool	53
5.4	The Common Astronomy Software Applications (CASA) Package	55
5.4.1	Coordinate System Support for Solar Images in CASA	55
6	References	58

1 INTRODUCTION

1.1 Purpose

This document represents the final report on the Development Plan Study "Solar Research with ALMA" (PI: R. Brajša, Hvar Observatory, Faculty of Geodesy, University of Zagreb, Croatia) in the framework of the ESO's "Advanced Study for Upgrades of the ALMA". The study was performed at the Czech ARC Node (Astronomical Institute of the Czech Academy of Sciences, Ondřejov, Czech Republic, PM: M. Bárta) in close collaboration with the corresponding North American Development Study "Advanced Solar Observing Techniques" (PI: T. S. Bastian, NRAO, Charlottesville, VA, USA), and related activities in East Asia. The goal of these activities was to implement, test and validate solar observations with ALMA.

1.2 Scope

The report summarizes commissioning work carried out to enable and validate ALMA solar observing modes. This includes development of solar observing modes, calibration procedures and tests, interferometric and single dish imaging tests and development of related software tools and methods for data reduction.

1.3 Related Documents

Most activity related to the implementation of solar observing modes is logged into JIRA tickets, many of which were referenced throughout the document. The most important JIRA tickets concerning solar observing are listed in Table 1. Note that some tickets contain many sub-tickets which are not listed in the table. Two papers by the Solar ALMA Development Team describing in detail the single-dish (White et al., 2017) and the interferometric (Shimojo et al., 2017) solar ALMA observations were recently submitted and accepted for publication. Also, the third paper about a comparison of solar ALMA observations and model based predictions of the brightness temperature was recently submitted (Brajša et al., 2017a). A detailed review of solar science that ALMA will be able to address was also published (Wedemeyer et al., 2016).

Table 1: Relevant JIRA tickets.

JIRA ticket	Description
CSV-239	Develop Fast-scanning Techniques for Obtaining Zero-spacing Continuum Data
CSV-2925	3 rd solar observing campaign in 2013
CSV-2933	Interferometric imaging with solar filters
CSV-3162	December 2014 Solar Campaign
CSV-3171	Examine the linearity of the receiver system with single-dish total power observations
CSV-3244	December 2015 Solar Campaign
SCIREQ-930	The ALMA solar ephemeris generator tool

1.4 Accomplishments

During the course of this project, several important accomplishments were achieved, the most important being that solar observations with ALMA are now offered to the solar science community. Below, all important accomplishments during this project are listed.

- **Solar CSV campaign in December 2014** - testing of the mixer-detuned modes in bands 3 and 6, single-dish fast-scanning modes, effect of MD modes on calibration. Team members R. Brajša and M. Bárta took part at that campaign.
- **Solar CSV campaign in December 2015** - based on the results from the previous campaign, several enhancements and optimizations were implemented into the solar observing workflow which are now used in regular solar observations. Single-dish tests of bands 7 and 9 and TDM spectral mode. Team member I. Skokić took part at that campaign.
- **Regular solar observations offered since Cycle 4 (2016)** - following the December 2015 CSV campaign, which also served as a dress-rehearsal for regular solar observing, solar observations were offered to the public for the first time in Cycle 4 Call for Proposals. Interest from the solar physics community was beyond expectations and over 50 proposals were submitted. **Regular solar observations started in December 2016** and the team member I. Skokić took part in that campaign. Also, a number of European solar facilities in the visible part of the spectrum were involved as the ground-based support during the December 2016 and March-April 2017 observing campaigns.
- **Press release (2017)** - two ALMA press releases about solar observing were simultaneously published on January 17, 2017, at ESO¹ and at NRAO². They were rather well received by the press and general public, both of which showed great interest, and a number of interviews were given by the solar development team members. Moreover, team members R. Brajša and I. Skokić were listed as contacts together with R. Hook at the ESO press release.
- **CSV data release (2017)** - a big part of CSV data from the solar campaigns in 2014 and 2015 was publicly released in January 2017 through the ALMA Science Verification Data web page³. These datasets include raw and calibrated data, reference images and calibration/imaging scripts of various solar targets including the quiet Sun regions, active regions, sunspots, limb and prominences, in bands 3 and 6.

1.5 Acknowledgments

This report summarizes activities aimed at enabling solar observations with ALMA performed by the ALMA Solar Development Team and collaborators. Solar Development Team is a small group of scientists and engineers led by Tim Bastian (NRAO), with Masumi Shimojo (NAOJ) leading the interferometric solar observing, Stephen White (AFRL) and Kazumasa Iwai (NAOJ) leading the single-dish solar observing and Ivica Skokić (Ondrejov) leading work on coordinate conversion and adjusting OT requirements. Most of the testing and commissioning work was coordinated by Tim Bastian, the PI of the North American ALMA Solar Development Plan.

We express special thanks to ALMA JAO, Antonio Hales, Tony Remijan, Akihiko Hirota, Neil Phillips, Itziar de Gregorio, Stuart Corder and Lars-Ake Nyman for their excellent

¹ <http://www.eso.org/public/news/eso1703/>

² <https://public.nrao.edu/news/2017-alma-solar-campaign/>

³ <https://almascience.eso.org/alma-data/science-verification>

support of the 2014 and 2015 solar observing campaigns and EOC testing; to colleagues from ESO, Pavel Yagoubov for his valuable work in developing mixer-detuned modes; Leonardo Testi, Robert Laing and Andy Biggs for fruitful discussions and support. We would also like to thank Richard Hills for broad input on a range of relevant topics and for his leadership in developing the fast-scanning mode, as well as IRIS (Bart de Pontieu), Hinode (A. Hosoi, T. Matsumoto, Y. Arikawa, T. Shimizu), NST (Dale Gary), Ondřejov, Hvar and Kazelhöhe observatories and their teams for their readiness in providing simultaneous observations in different spectral ranges. Finally, we thank Sven Wedemeyer & S-SALMON Network for organising and collecting input from solar-physics community world-wide which resulted in an extended set of ALMA solar science cases published in Space Science Reviews (Wedemeyer et al., 2016).

We additionally thank the following individuals for their efforts in supporting ALMA solar development, listed alphabetically: Arnold O. Benz, Bin Chen, Mateja Dumbović, Dale Gary, Gregory Fleishman, Arnold Hanslmeier, Hugh Hudson, Gordon Hurford, Adam Kobelski, Donghao Liu, Maria Loukitcheva, Sujin Kim, Sam Krucker, Matej Kuhar, Ivana Poljančič Beljan, Drago Roša, Pascal Saint-Hilaire, Davor Sudar, Yihua Yan, Sijie Yu. Finally we thank ESO for its support of the ALMA solar development plan study entitled “Solar Research with ALMA” (PI R. Brajša), the NSF for its support of the companion study entitled “Advanced Solar Observing Techniques” (PI T. S. Bastian), and the Astronomical Institute of the Czech Academy of Sciences, Ondřejov for providing infrastructure and resources for the present study and the Czech ARC Node.

2 SOLAR OBSERVING MODES

ALMA was designed for observing a wide range of millimeter/sub-millimeter targets, from solar system objects to distant galaxies. The Sun is far brighter at these wavelengths than other ALMA targets and many solar phenomena appear on very short time scales. Solar interferometric observations are especially difficult because the Sun fills the beam of the ALMA antennas with structures over a wide range of spatial and temporal scales. All these facts impose significant constraints on observing modes and calibration strategy for successful solar observations.

ALMA antennas were designed from the beginning to protect the sensitive detectors from the strong solar flux and heat load. The antenna surfaces are designed to scatter optical/IR radiation, while focusing (sub)millimeter wavelengths. However, additional measures are needed for useful observations of the Sun. ALMA receivers are designed for a maximum RF signal corresponding to an effective brightness of about 800 K at the receiver input, which is 5-10 times less than the quiet Sun temperature at ALMA frequencies. Therefore, the solar signal must be attenuated or the receiver gain must be reduced to ensure the proper dynamic range.

2.1 Solar Filters

The initial solution adopted by ALMA was the use of a “solar filter” (SF) mounted on the Amplitude Calibration Device (ACD) of each antenna. When placed in the optical path the solar filter is required to attenuate the signal by $4+2\lambda_{\text{mm}}$ dB with a return loss of -25 dB (-20 dB for frequencies higher than 400 GHz) and a cross polarization induced by the filter of -15 dB, or less. There are several drawbacks to this solution:

- The hot and ambient calibration loads cannot be observed when the SF is in the optical path, making amplitude calibration difficult
- The SNR on calibrator sources is greatly reduced, not just by the attenuation introduced by the filter, but by the thermal noise that is added to T_{sys} by the filter itself
- The SFs must be moved out of the beam when observing calibrators, thereby increasing operational overhead
- The SF introduces frequency dependent (complex) gain changes that may be time dependent and must be calibrated
- The SFs introduce significant wave-front errors into the illumination pattern on the antenna, resulting in distortions to the beam shape and increased side lobes
- The Water Vapor Radiometers (WVRs) are blocked by the ACD for many bands when the SF is inserted into the optical path and phase corrections based on WVR measurements are therefore not possible in these bands

Some of these difficulties have been overcome – e.g., the complex gains of antennas outfitted with SFs were measured during the 3rd solar observing campaign in 2013 (CSV-2925) – and interferometric imaging with solar filters has been demonstrated (CSV-2933). In fact, the SFs may be used for observation of solar flares at some future time. Nevertheless, the disadvantages of the usage of solar filters are significant.

2.2 Mixer Detuning

While solar filters have been demonstrated to work, their disadvantages led to an alternative approach. Yagoubov (2013) showed that the ALMA SIS mixers could be de-tuned or de-biased to reduce the mixer gain and effectively increase the saturation level to allow solar observing without the use of the solar filters, at least for non-flaring conditions on the Sun. This is illustrated in Figure 1, which shows the SIS current (left axis) and conversion gain (right axis) plotted against the voltage bias for Bands 3 and 6. The normal voltage bias tuning is on the first photon step where the gain conversion is maximal. However, the mixer still operates at other voltage bias settings. These produce lower conversion gain but since the dynamic range scales roughly inversely with gain, these settings can handle large signal levels before saturating. In addition to the SIS bias voltage, the local oscillator (LO) power can be altered in order to further modify the receiver performance.

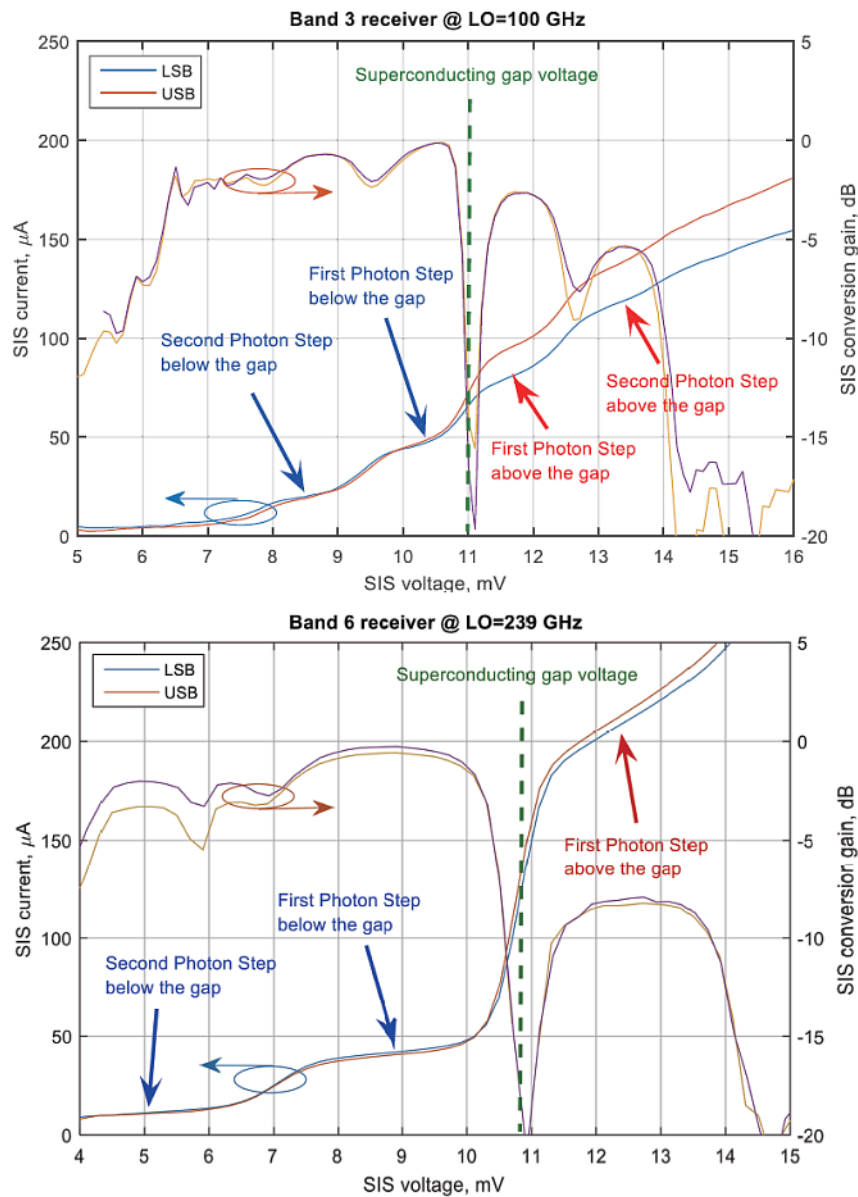


Figure 1: SIS mixer current and conversion gain as a function of bias voltage. Ellipses with arrows (red and blue) denote relevant ordinate axis (from Shimojo et al. 2017).

Laboratory tests by P. Yagoubov on band 5 in late 2013 and early 2014 were sufficiently encouraging to perform tests on antennas at the ALMA site. These were executed in 2014-2016 for additional bands, namely 3, 6, 7 and 9. Results are summarized in Table 2.

Two mixer detuned (MD) modes are available, MD1 which was designed for observing quiet Sun regions, and MD2, designed for higher brightness solar phenomena like active regions and flares. The receiver sensitivity is usually degraded in the detuned mode, with noise temperature typically in the range 100 – 1000 K. While in bands 7 and 9 both modes use the same parameters and are, in fact, the same, in bands 3 and 6 MD2 has lower sensitivity but also lower compression compared to MD1. If high sensitivity with better flux calibration is needed, MD1 mode could be used and calibrated by MD2 mode. Additionally, it should be possible to optimize between receivers’ linearity and sensitivity by tuning the LO power.

Table 2: Recommended local oscillator (LO) and SIS mixer settings for bands 3, 6, 7 and 9. Nominal LO power refers to LO power as set by ALMA software for standard observations (Yagoubov 2016).

Band	Mode	LO power	SIS bias [mV]	Compression with quiet Sun input [%]	Receiver noise [K]	Antenna temperature [K]	Sun temperature [K]
3	MD1	nominal	8.5	~10	~50	5800±250	6500±250
	MD2	nominal	13.3	< 5	~800	6250±200	7000±200
6	MD1	nominal	9.3	~10	~60	4600±350	5350±350
	MD2	nominal	12.5	< 5	~800	5000±200	5800±200
7	MD1	nominal	3.5	< 5	~2000	3800±200	4800±200
	MD2	nominal	3.5	< 5	~2000	3800±200	4800±200
9	MD1	nominal	1.9	< 5	~100	2200±200	4500±200
	MD2	nominal	1.9	< 5	~100	2200±200	4500±200

Band 7 shows a significant receiver noise temperature around 2000 K for the recommended 1st photon step above the gap. The main problem with the 1st photon step below the gap (which has smaller receiver noise) is the linearity and calibration accuracy due to limited range of flat gain response. An additional calibration step might be implemented to transfer flux calibration from the 1st photon step above to the one below the gap to solve the issue with the high receiver noise.

The advantages of the MD modes are numerous, perhaps the most prominent one being that observations of both the Sun and calibrators can be made without moving the solar filter in and out of the optical path and managing the complexity and overhead associated with calibration when using solar filters. Nevertheless, there are additional considerations when using MD modes.

2.3 Linearity of the MD Modes

An important issue for calibration is whether the detuned receiver modes put solar observations in a linear regime. The linearity of the receiver system was examined using the Sun itself with single-dish total power observations (CSV-3171; Iwai, 2016a). We observed the Sun using different tuning conditions almost simultaneously. We assumed that the SIS device outputs a lower signal power under conditions for which the gain has been reduced. For example, if we input the same signal, the output level of the MD2 mode should be lower than that of the MD1 mode. Hence, if two output levels derived under different tuning conditions exhibit linearity, this indicates that neither mode is saturated. Figure 2 shows the scatter plots obtained for scans across the Sun using the nominal (“normal”) SIS mixer

tunings, the MD1 tuning, and the MD2 tuning for bands 3 and 6. The red and green lines show the fitting results obtained using a signal derived inside the disc region and off the solar limb, respectively. The scatter plots are obtained by plotting normal, MD1, and MD2 modes against each other. We conclude from these that the normal, MD1, and MD2 modes are linear for the purposes of calibration and off-limb pointing, but are in saturation when pointing at the solar disk, displaying moderate compression. If we assume that the MD2 mode of band 3 is not saturated, the MD1 mode underestimates the actual solar level by about 12%. Similar results are obtained for band 6 (13%).

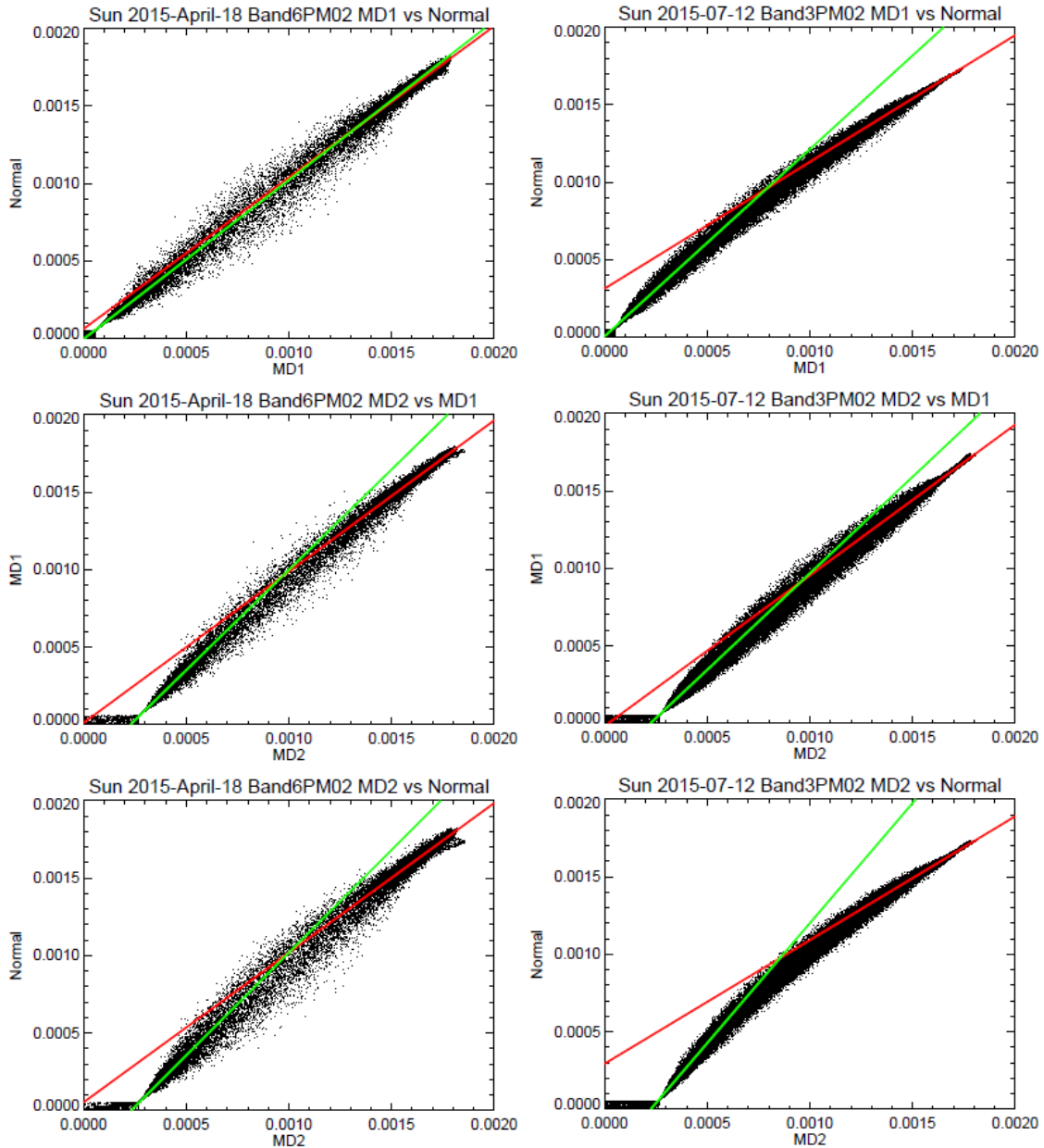


Figure 2: Scatter plots of solar output levels for two different mixer modes of Band 6 (left) and Band 3 (right): Normal and MD1 (top); MD1 and MD2 (middle); and MD2 and Normal (bottom). The red and green lines show the fitting results obtained using a signal derived inside the disc region and outside the limb, respectively (Iwai, 2016a).

From these results, we recommend using the MD2 mode for single dish observations. Although the MD2 mode is likely not saturated, its linearity should be confirmed by cross-

comparison with an MD mode that reduces the gain still further (MD3), which is planned for the upcoming solar observing campaigns.

2.4 IF Attenuator Settings

While both calibrators and the Sun can be observed in an MD mode, the power entering the system when observing a calibrator and the power entering the system when observing the Sun are vastly different. The ALMA analog-to-digital converters (ADCs) are sensitive to input power which has to be adjusted to the ADC optimum values (the recommended input level is 3.8 dBm) through the use of stepped attenuators under digital control. The IF chain has two variable attenuators (in steps of 0.5 dB) to ensure that signal levels remain within nominal limits: one in the IF Switch and one in the IF Processor. However, when the levels of the attenuators in the IF Switch and IF Processor are optimized for the Sun, they are non-optimum for calibrator sources. It is necessary to reduce the attenuation levels relative to the solar values when observing phase and flux calibrators.

Table 3: Attenuator levels for calibrators for different detuning modes in bands 3 and 6 (Shimojo et al. 2017).

		Difference in Attenuator Levels		Input Level to ADCs	
Receiver	MD mode	IF Switch	IF Proc	Sun	Calibrator (sky)
Band3	MD1	-8 dB	-10 dB	≈3.5 dBm	≈3.5 dBm
	MD2	-8 dB	0 dB	≈3 dBm	≈4 dBm
Band6	MD1	-10 dB	-10 dB	≈3.5 dBm	≈2.5 dBm
	MD2	-8 dB	0 dB	≈4 dBm	≈4.5 dBm

Extensive tests were carried out in 2014 to determine the appropriate attenuator values. The stepped attenuators were set to values that optimized ADC signal input levels when observing the Sun and then they were adjusted to levels appropriate for calibrator observations. The resulting values are listed in Table 3.

2.5 Water Vapor Radiometers

In MD mode, there is no blocking of the WVRs by the ACD, thereby allowing phase corrections to be made for each 12 m antenna – at least in principle. When pointing to the Sun, the radiometer signal will be

$$T_{in} = \eta_b T_{sun} e^{-\tau} + \eta_c T_{atm} (1 - e^{-\tau}) + (1 - \eta_c) T_{amb} \quad (1)$$

where T_{sun} is the brightness temperature of the Sun, T_{atm} and T_{amb} are the temperatures of the atmosphere and the ambient at the telescope, respectively, and η_c the beam coupling efficiency between the radiometer and the sky and η_b is the fraction of the coupling of the radiometer to the disc of the Sun. We have $T_{sun} \gg T_{atm}, T_{amb}$ and with $\eta_b \approx \eta_c$ the first term dominates. The water vapor line is therefore seen in absorption against the Sun in contrast to the usual case where the line is observed in emission. While this is not a problem, the use of the WVRs for solar observing would require changes in the implementation of the WVR correction to the data. This has not been considered in detail because a much more serious problem is that, currently, the WVRs saturate when pointed at the Sun. They are designed to

operate over an input range of ~ 30 K (cold sky) to ~ 350 K (internal WVR hot load), with a specification that they should operate up to ~ 600 K. Unless the optical depth of the sky is ~ 2.5 or more, which would represent highly non-optimum observing conditions in any case, the WVRs are expected to saturate on the Sun. This was checked in March 2014 and the WVRs were indeed found to be in strong saturation on the Sun. Unless the WVRs are modified or replaced to increase their dynamic range to accommodate the Sun, phase corrections based on WVR measurements will not generally be possible when pointed at the Sun.

Therefore, currently the WVRs cannot be used to correct solar data for phase variations introduced by water vapor along each antennas line of sight, regardless of whether the solar filters or the MD modes are used. As a consequence, solar observations will be largely confined to the use of compact antenna configurations. Also, since Cycle 3, perceptible water vapor (PWV) correction is applied on-line as a normal operation, so in solar case it should be disabled.

2.6 Choice of Frequencies

A set of default LO frequencies within ALMA bands was proposed (Hills, 2015) so that the same setups were used for various tests and early solar observing. The frequencies were chosen so that they are reasonably close to the middle of each band where the atmospheric absorption is low, also to include recombination lines, if possible, for spectral line observations, and that sideband ratio (in some bands) can be used for phase correction.

Table 4: Proposed LO frequencies for solar observations (Hills, 2015)

Band	3	4	5	6	7	8	9	10
LO frequency (GHz)	100	152	194	239	336	416	669	861

In contrast to non-solar observations where the observing frequencies can be selected anywhere within the observing frequency range of allowed bands, the observing frequencies for the solar observations in Cycles 4 and 5 are restricted to those listed in Table 5 because the performance of the MD modes has not been tested and validated across the entire frequency range yet. We do not expect this to be a limitation on the achievable science since solar observations are restricted to continuum (in effect, low spectral resolution) measurements for which the chosen frequencies should be sufficient. This restriction will be removed in future.

Table 5: Allowed frequencies for solar observations in Cycles 4 and 5

Band	LO Freq.	LSB		USB	
		BB1	BB2	BB3	BB4
Band 3	100 GHz	92-94 GHz	94-96 GHz	104-106 GHz	106-108 GHz
Band 6	239 GHz	229-231 GHz	231-233 GHz	245-247 GHz	247-249 GHz

Similarly, the baseline correlator mode in Cycles 4 and 5 is fixed to the Time Domain Mode (TDM). The Frequency Domain Mode (FDM) may be available in Cycle 6 or beyond. Some spectral line tests were performed during December 2015 campaign both with single dish and interferometric observations, but they were unsuccessful.

2.7 Spatial Scales

The Sun is a very difficult object to observe with an interferometer because it fills any ALMA field of view with emission on a wide range of spatial scales, from the large-scale background

down to the smallest magnetic field structures. On the other hand, interferometers sample a fixed range of spatial scales corresponding to the different baselines they cover. In radio interferometry, Earth rotation is usually used to increase the effective number of baselines, but this method is not useful for solar observing since solar phenomena are very dynamic and rapidly changing.

To ensure time synchronization of the data and to obtain good u-v coverage, the heterogeneous array formed from 12m- and 7m-antennas is required for solar observations. That is, all 7m- and 12m-antennas of the array are connected to the Baseline Correlator. The use of the heterogeneous array for solar observations has been validated during the last several solar campaigns.

The use of single dish measurements to recover absolute flux measurements and missing u-v spacings corresponding to large-scale structures has already been emphasized. However, the most striking proof for combining single dish and interferometric measurements can be seen in Figure 3. It clearly shows that SD image is essential, not only for deriving the absolute brightness, but also to identify large scale structures.

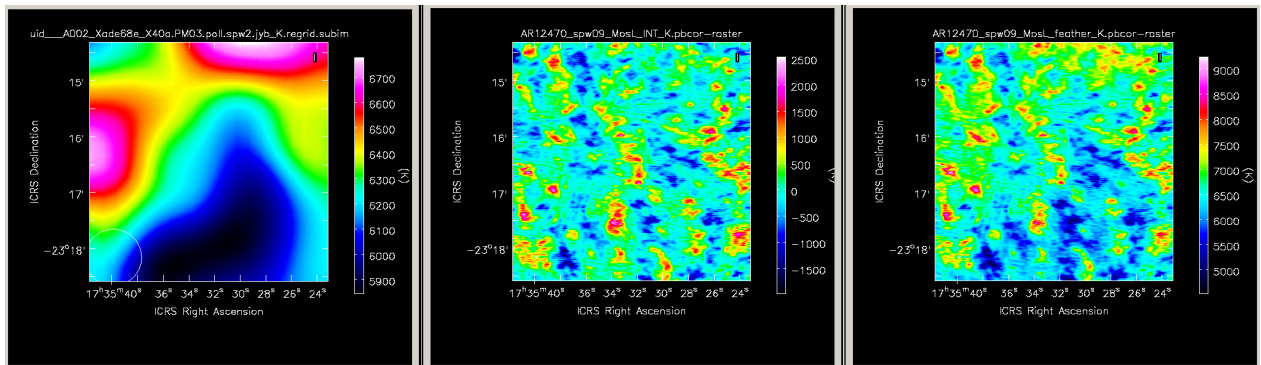


Figure 3: The effect of combining single dish (left) and interferometric (middle) measurements to obtain the final image (right) using "feathering". The measurements were made during December 2015 campaign.

2.8 Calibrator Selection

Since the MD mode reduces the sensitivity of the receiver, the criterion for selecting calibrators for non-solar observations cannot be used for solar observations. The flux of phase and flux calibrators has to be >1 Jy with sources >2 Jy preferred. The brightest quasar available will be selected as a bandpass calibrator. The bandpass calibrator is used to check the soundness of the flux calibration so it must not be the same as the flux calibrator. The calibrator should be located at least 2 degrees away from the Sun to minimize the effects of sidelobes.

The distribution of bright quasars suitable for calibration in Band 6 is shown in Figure 4. A similar situation is for the Band 3. There is a period in early July when there are no bright calibrators within 20 degrees from the Sun, so solar observations should be avoided at that time, especially in bands higher than 3.

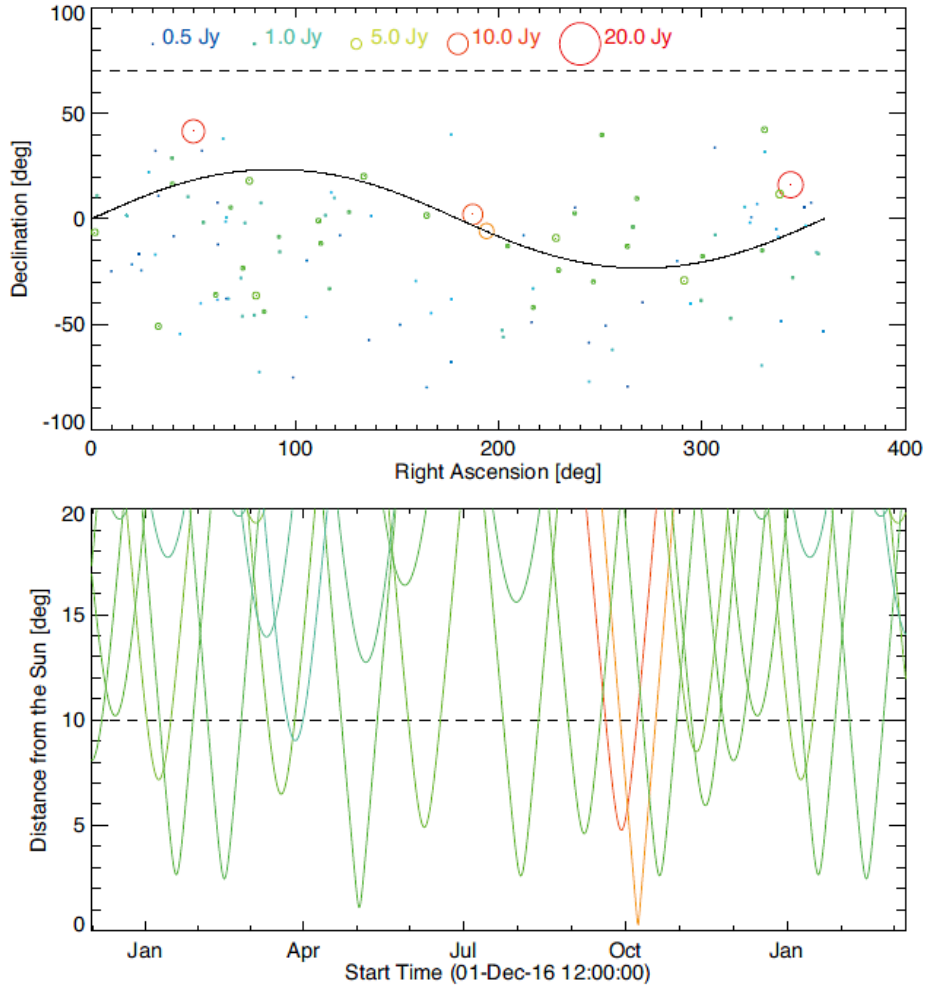


Figure 4: Upper panel: The distribution of the quasars brighter than 0.5 Jy in Band 6. The color and size of the circle indicates the flux of a quasar. The black line indicates the track of the Sun. Lower panel: The separation angle between the Sun and possible calibrator sources (>1 Jy). The color indicates the flux of a quasar (same as that used in the upper panel)(Shimojo et al. 2017).

2.9 Time and Scheduling Constraints

Several facts influence the scheduling of solar observations. Since WVR correction is currently not available in solar case, compact antenna configurations are favored. In Cycles 4 and 5, the three shortest array configurations (Cnn-1, Cnn-2, and Cnn-3) will be used for solar observations, limiting the observing season to the period when these configurations are available. Therefore, solar observations will be presently held in campaign mode.

Several limitations impose constraints on available time period and scheduling of solar observations. At low solar elevations (<40 degrees), due to close proximity of the 7-meter antennas in the ACA array, antenna shadowing occurs, limiting the observations to the following periods:

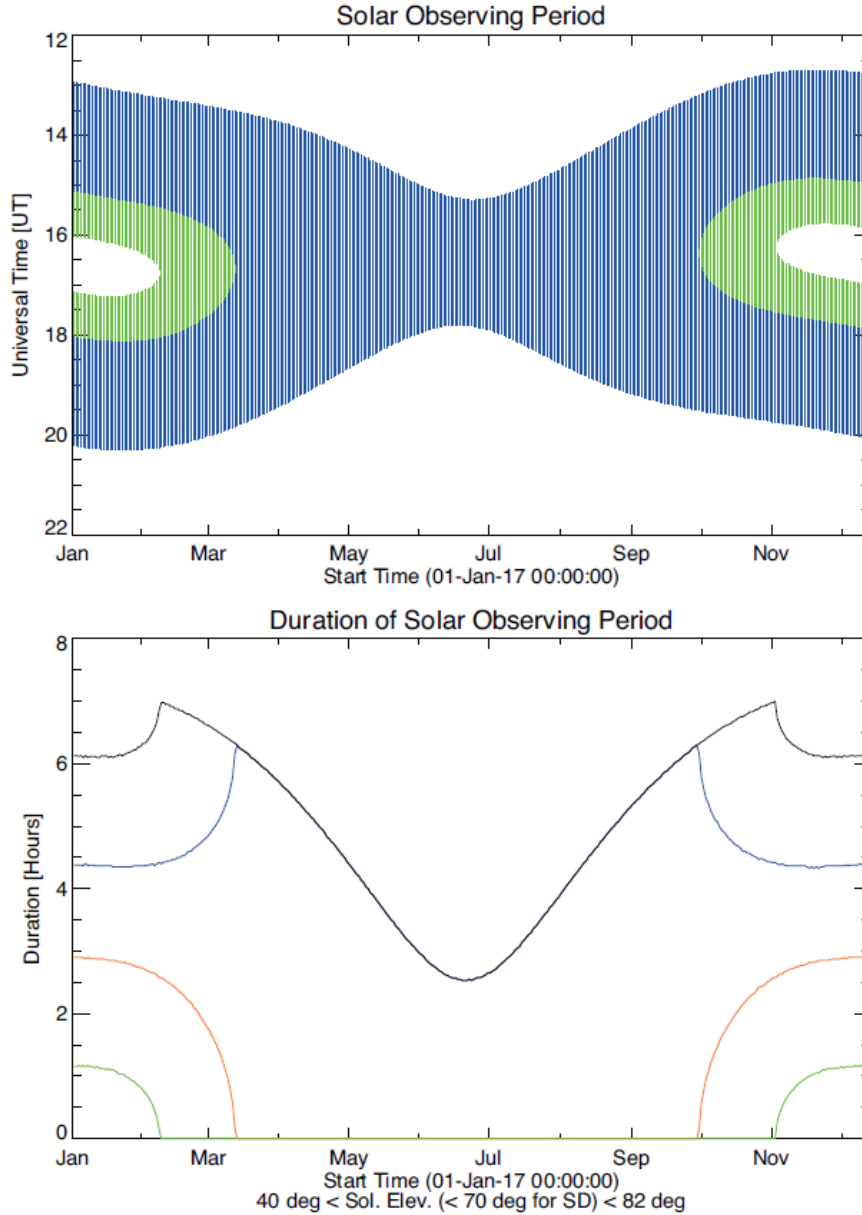


Figure 5: The temporal range of solar observations. Upper panel: The blue lines indicate the possible temporal ranges of solar observations with both heterogeneous and Total-Power (TP) arrays. The green regions show the time range when we can use only heterogeneous array. Lower panel: Black line indicates the total duration of the solar observing with heterogeneous array in a day. Blue line shows the total duration of the solar observing with TP array in a day. Orange and green lines show the lost time caused by high elevation of the Sun (Orange: $>70^\circ$, Green: $>82^\circ$)(Shimojo et al. 2017).

- Summer Solstice [in December]: 13:00~20:00UT (10:00~17:00 CLT)
- Fall/Spring Equinox: 13:30~19:30UT (10:30~16:30 CLT)
- Winter Solstice [in June] 15:30~17:30UT (12:30~15:30 CLT)

ALMA antennas cannot track the Sun when it is near the zenith due to antenna azimuthal drive slewing limits which means that solar observations cannot be performed when the Sun is higher than 70 degrees (for single-dish fast scanning) and 82 degrees (for interferometric observing). The available windows for solar observing and their duration during the year are shown in Figure 5.

Another scheduling constraint is important to note, and it is related to the unpredictable and fast-changing nature of solar features like active regions, filaments and flares. It is impossible to predict weeks or months in advance the appearance and visibility of the solar phenomena, and their exact position needed for small FoV of ALMA antennas. The ALMA Ephemeris Generator was developed to predict the position a few days in advance. However, the Principal Investigator (PI) still needs to submit the target coordinates at least 24 hours prior the scheduled observation. To successfully perform such solar observation, close cooperation between Contact Scientist, Astronomer On Duty and PI is needed.

2.10 Joint Observations

To maximize scientific output from ALMA, joint simultaneous observations with other satellite and ground-based instruments (IRIS, Hinode, ChroTel, NST, etc.) are essential. For successful coordination of joint observations, the PI and teams need to know the week of observation at least one month before (although it is possible for some instruments to be at disposal only a few days before the observation). One month constraint is needed also in case of non-joint observations to avoid the miscommunication between the PI and ALMA operation team, regarding the pointing and ephemeris.

3 INTERFEROMETRIC SOLAR OBSERVING

In this chapter we describe the current implementation of ALMA solar interferometric observing. Being a somewhat special and difficult ALMA target, observing the Sun includes (near) simultaneous usage of all available antennas, from the main 12-meter array, the compact 7-meter array and total power array. To get as many baselines as possible to achieve successful imaging of solar targets, both main and compact arrays are connected to the baseline correlator as heterogeneous array. However, total power array antennas are not, and they are used separately to get single-dish full disk solar images which are later combined with interferometer data during imaging process in software. The focus of this chapter is interferometric observing, while total power single-dish observations are described in the next chapter.

3.1 Validation of Interferometric Observations

Before investing substantial time in testing MD modes for solar observing, interferometric observing was validated under controlled conditions through computation of closure quantities. These were performed in 2014 under JIRA ticket CSV-3105. A calibrator source was observed with both nominal SIS mixer settings and with MD settings. Phase closure is illustrated in Figure 6. The first three panels show the raw visibility phases on three baselines, formed by three antennas, for a calibrator source (1924-292) observed in band 6. The first, second, and fourth scans were made with nominal SIS mixer settings and the third scan was made with MD2 SIS mixer settings. The fourth panel shows the closure phase formed by the three antennas which, despite the larger scatter because of the lower gain and enhanced system temperature, is consistent with zero.

Similarly, amplitude closure is illustrated in Figure 7, where the raw amplitudes on four baselines are shown along with the amplitude closure in the bottom panel. Again, the scatter is increased, but the closure amplitude is unity. Given the obvious difference in the complex gain of each antenna when switching between nominal and MD mixer settings, it is highly desirable to observe both calibrators and the Sun in a fixed MD mode. Otherwise, the differential gain between the nominal and MD observing mode would need to be measured and applied every time solar observations were performed, perhaps repeatedly during a solar observation.

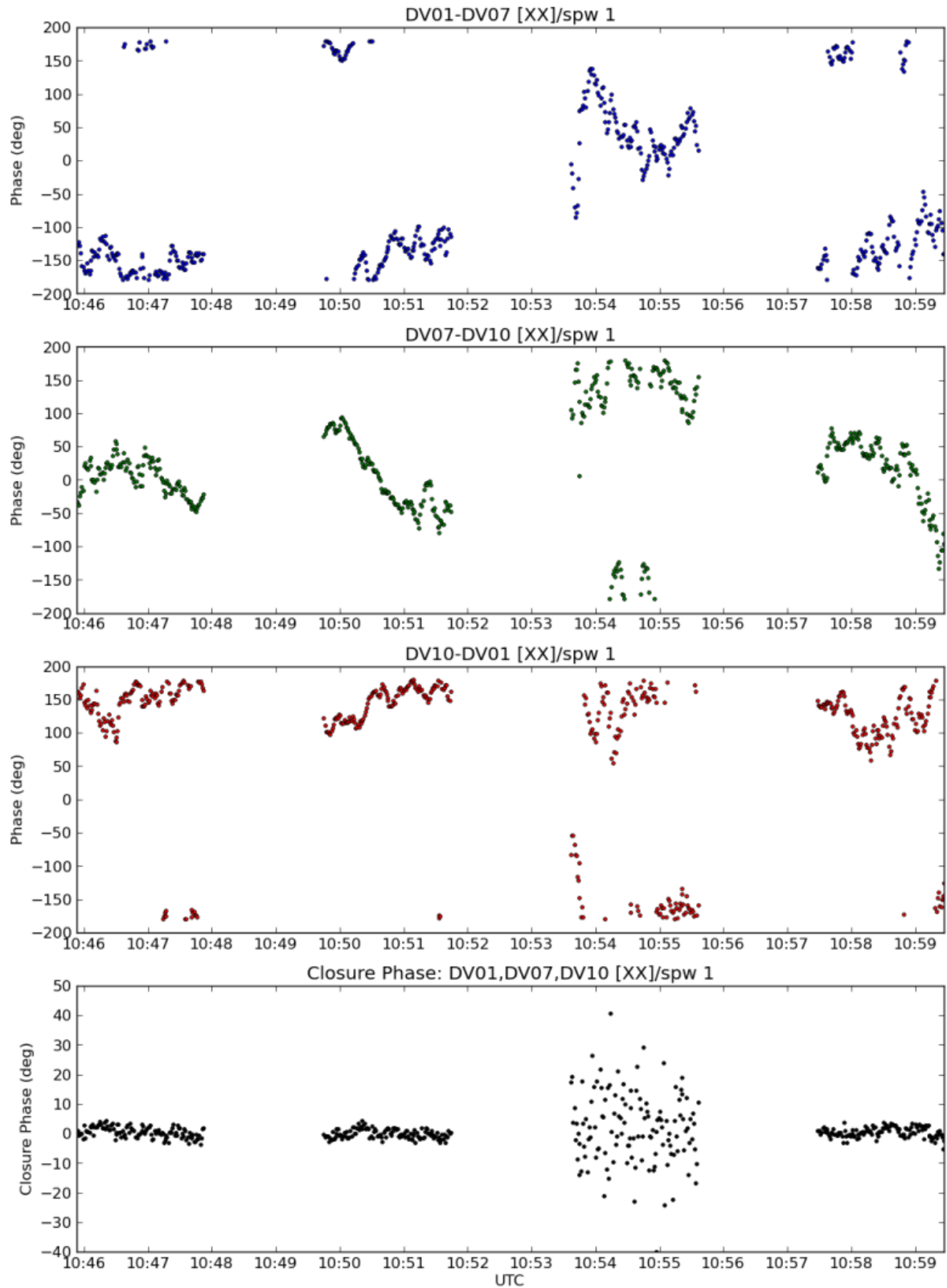


Figure 6: The top three panels show the visibility phase between DV01-DV07, DV07-DV10, and DV10-DV01, respectively. Phase closure between DV01, DV07, and DV10 is shown in the bottom panel using data obtained in band 6 using both nominal receiver settings (scans 1, 2, and 4) and MD2 receiver settings (scan 3). (Data: uid://A002/X8b8415/Xd4f)

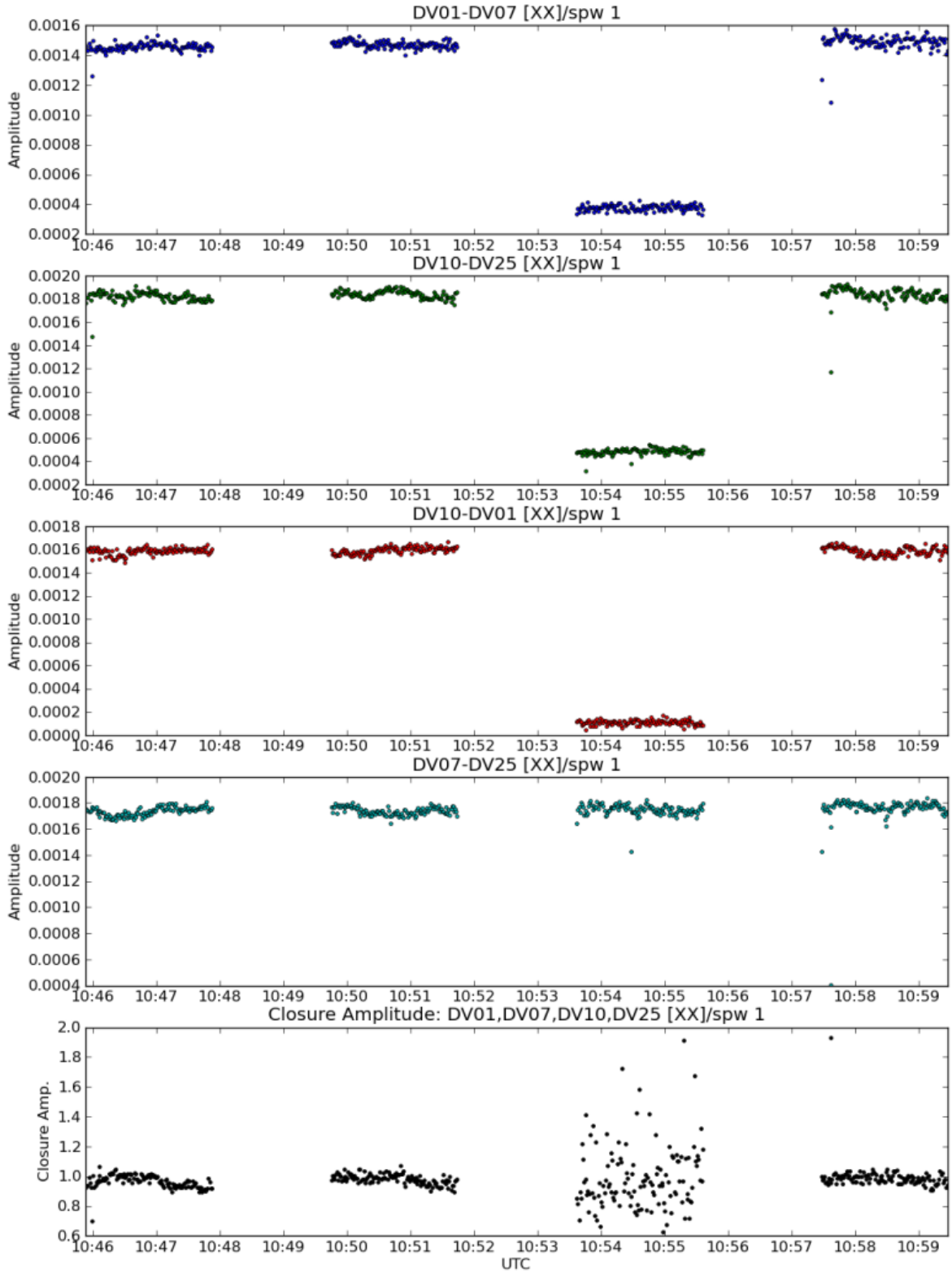


Figure 7: The top three panels show the visibility amplitude between DV01-DV07, DV10-DV25, DV10-DV01, and DV07-DV25, respectively. Amplitude closure between DV01, DV07, DV10, and DV25 is shown in the bottom panel using data obtained in band 6 using both nominal receiver settings (scans 1, 2, and 4) and MD2 receiver settings (scan 3). (Data: uid://A002/X8b8415/Xd4f)

3.2 Phase Calibration Transfer

The variation in system temperature caused by the stepped attenuators is negligibly small, so we do not need to correct for their influence on flux calibration. On the other hand, the attenuators do introduce phase shifts (Figure 8), depending on the difference in attenuation introduced for solar and calibrator scans. If the values of the phase shifts in all antennas are identical, the phase shift will be differenced out and the transfer of phase calibration from a calibrator to the solar source can proceed without the added complexity of measuring and applying differential phase corrections to account for phase errors introduced by the IF Switch and IF Processor attenuators.

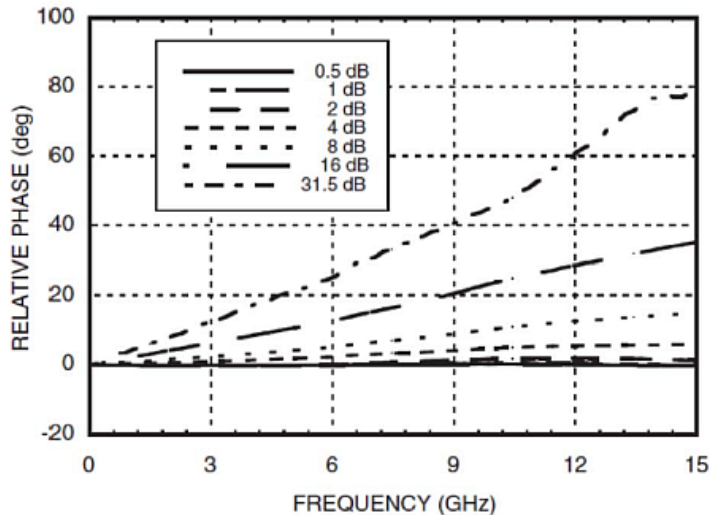


Figure 8: Phase change introduced by attenuator states ranging from 0.5-31.5 dB.

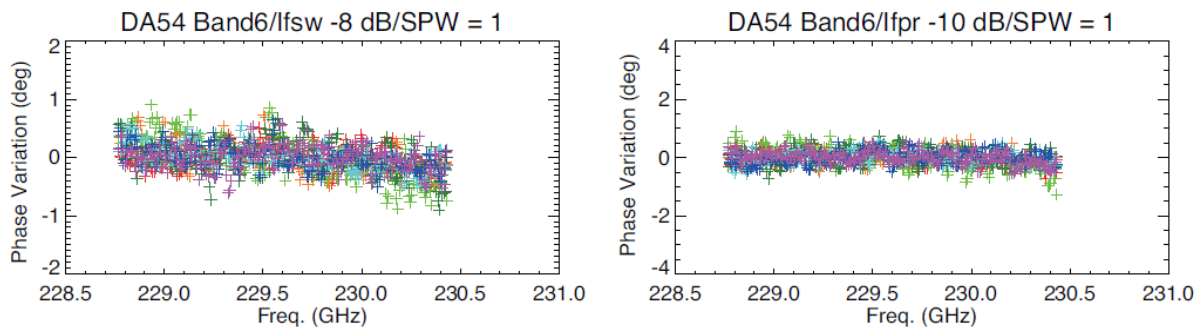


Figure 9: The differential phase variation in Band 6. Attenuator levels were changed from the state optimized for solar observing by -8 dB in IF Switch (left) and -10 dB in IF Proc (right) for calibrator measurements. Colors indicate different observing days in period December 14-20, 2015 (Shimojo et al. 2017).

To evaluate whether the attenuators introduced unacceptable differential phase errors or not, bright quasars were observed while changing the attenuation levels in both the IF Switch and/or IF Processor attenuators in an extensive series of tests during the December 2014 and December 2015 solar observing campaigns. These are documented in JIRA tickets CSV-3162, CSV-3244 and CSV-3165. Tests were performed using nominal, MD1, and MD2 settings for both band 3 and band 6. These tests demonstrated that the differential phases introduced by changes to attenuator settings were generally small, at least on short baselines (Figure 9). The situation was less clear on longer baselines, in part because the time between ATT state changes was rather long (220 s) and the long baselines are more susceptible to changes in the atmosphere.

In Band 6, MD2 mode may sometimes be too much attenuated to observe the calibrators, depending on the season and the number of suitable calibrators. In December 2015 a series of tests was performed to find an effect of switching between the MD2 and normal mode on the phase shift (documented under CSV-3251). The channel-averaged phase shift is close to zero, with a standard deviation of ± 3 degrees.

3.3 Bandpass Calibration

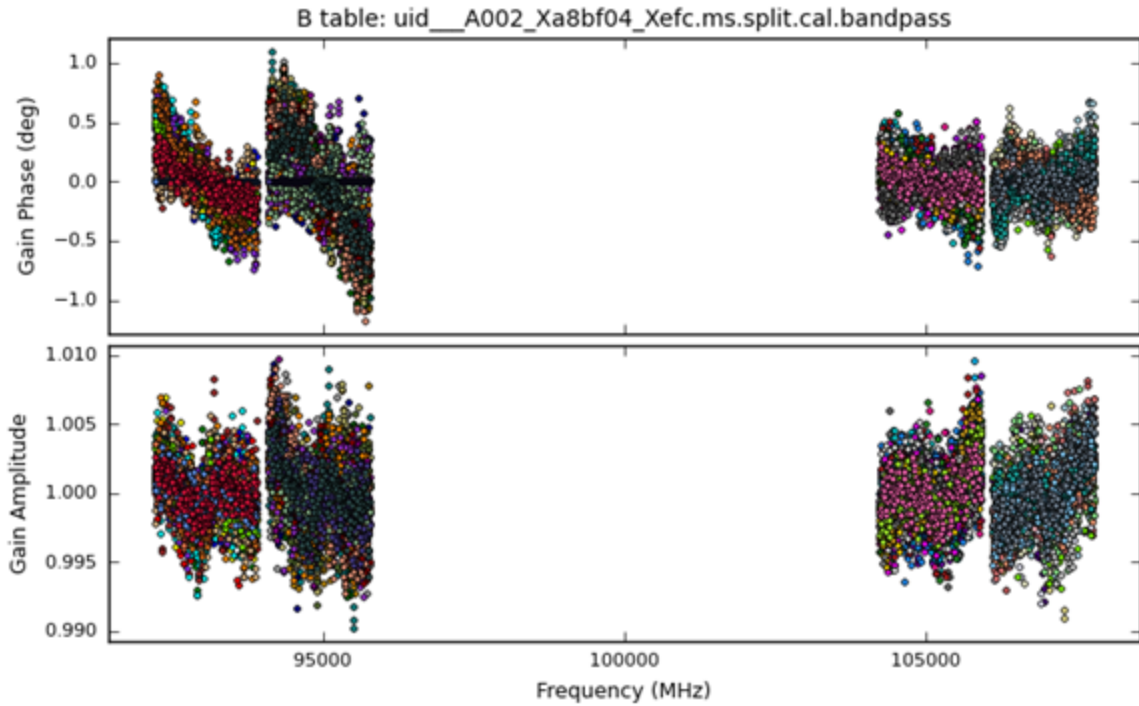


Figure 10: The residual of the differential phase and the variation of the amplitude for the upper and lower sidebands of band 3. The plot shows the case where the IF Switch attenuator has been reduced, i.e., the setting for the MD mode. (uid://A002/Xa8bf04/Xefc)

Bandpass calibration is carried out in the usual manner even when solar MD observing modes are used: i.e., a strong calibrator is observed in an MD mode with the attenuator levels optimized for the Sun and the bandpass solution is obtained. The bandpass shape and stability were checked for the MD modes and attenuator states. It was found that the perturbations to bandpass amplitudes and phases were small. For the IF-switch and IF-processor attenuator settings adopted for observations with an MD mode, it was found that the RMS difference between bandpass phases for an attenuator state and the nominal attenuator state was generally a fraction of a degree for both the Band 3 and Band 6 receivers, the maximum being 1.2 degrees (Figure 10). Similarly, the normalized amplitude difference was typically a fraction of 1%. We conclude that no explicit correction is needed to normal bandpass calibration as a result of using MD modes or different attenuator states when observing calibrator sources and the Sun.

3.4 Amplitude Calibration

The standard ALMA amplitude and flux calibration does not apply to solar data and should be modified. The reason for this is that antenna temperature T_{ant} , which indicates the input power from the target source, is significantly larger than the receiver system noise temperature T_{sys} when observing the Sun, so both have to be measured accurately. Moreover, the Sun is not a point-like source, it fills the field of view and even sidelobes with radiation.

For a typical ALMA astronomical observation, the output from the correlator is a normalized cross-correlation coefficient ρ_{mn} for a pair of antennas m and n :

$$\rho_{mn} = \frac{\sqrt{T_{corr_m} T_{corr_n}}}{\sqrt{(T_{ant_m} + T_{sys_m})(T_{ant_n} + T_{sys_n})}} \quad (2)$$

where T_{ant} is the antenna temperature, T_{sys} is the system temperature, and T_{corr} is the temperature of the correlated component of $T_{ant} + T_{sys}$. The relation between antenna temperature (in K) and flux density (in $\text{W Hz}^{-1} \text{m}^{-2}$) is:

$$T_{ant} = \frac{SA_e}{2k} \quad (3)$$

where k is the Boltzmann constant and A_e is the effective antenna collecting area (in m^2). The relation is also valid for the correlated component. The amplitude of a visibility measurement is:

$$S_{corr_{mn}} = 2k \frac{\sqrt{(T_{ant_m} + T_{sys_m})(T_{ant_n} + T_{sys_n})}}{\sqrt{A_{e_m} A_{e_n}}} \rho_{mn} \quad (4)$$

A System Equivalent Flux Density (SEFD) is defined as:

$$SEFD = 2k \frac{T_{sys}}{A_e} \quad (5)$$

Then, the amplitude of a visibility can be written as:

$$S_{corr_{mn}} = \rho_{mn} \sqrt{SEFD_m SEFD_n} \sqrt{(1 + q_m)(1 + q_n)} \quad (6)$$

where $q = T_{ant}/T_{sys}$. The antenna temperature of most celestial sources is much smaller than the system temperature, $T_{ant} \ll T_{sys}$, and $q = 0$. This is the case for calibrator sources which only need measurements of T_{sys} to scale the visibilities. In contrast, when observing the Sun $T_{ant} > T_{sys}$, and it is therefore necessary to measure both T_{sys} and T_{ant} in order to correctly scale the visibility measurements. The procedure for measuring T_{ant} and T_{sys} is described in detail in section on single-dish solar observing calibration. Briefly, the antenna temperature is measured using the ACD on which hot and cold load reference inputs are available. The following measurements are performed before each source scan:

- cold load observation P_{cold} (also known as the ambient load)
- hot-load observation P_{hot} , in which a heated absorber fills the beam path

- sky observation P_{sky} , offset from the Sun (typically by two degrees) and at the same elevation. The attenuation levels of the attenuators in IF chain are the same as that for the measurement of P_{cold} and P_{hot}
- off observation P_{off} , which is the same as the P_{sky} , except the attenuation levels are set to the values optimized for the Sun
- Sun observation P_{sun} , which is at the attenuation levels of the target (Sun)
- zero level measurement P_{zero} , which reports the levels in the detectors when no power is being supplied

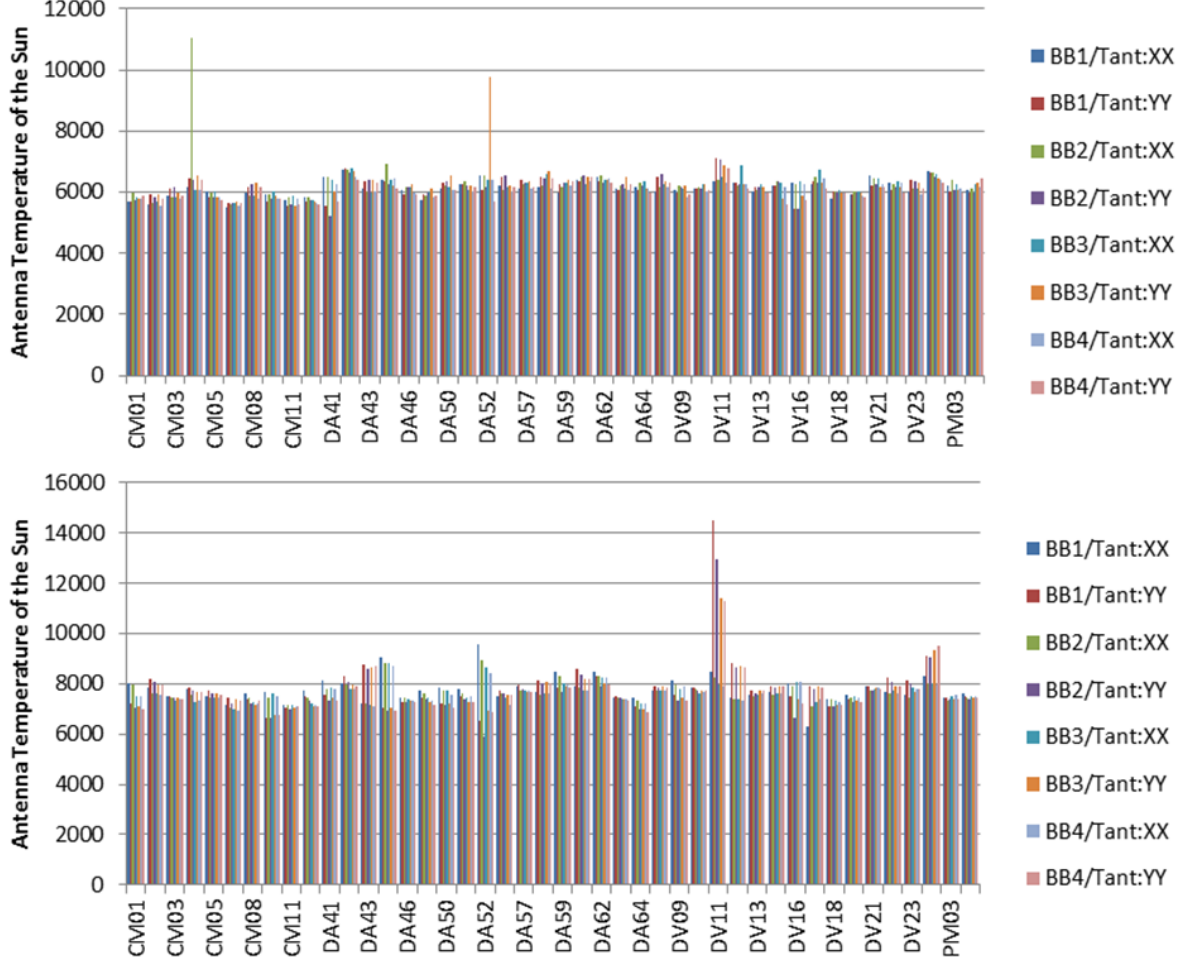


Figure 11: The antenna temperature of each antenna for band 3 MD1 (upper panel, uid://A002/Xa72fea/Xf1e) and MD2 (lower panel, uid://A002/Xa72fea/Xd96).

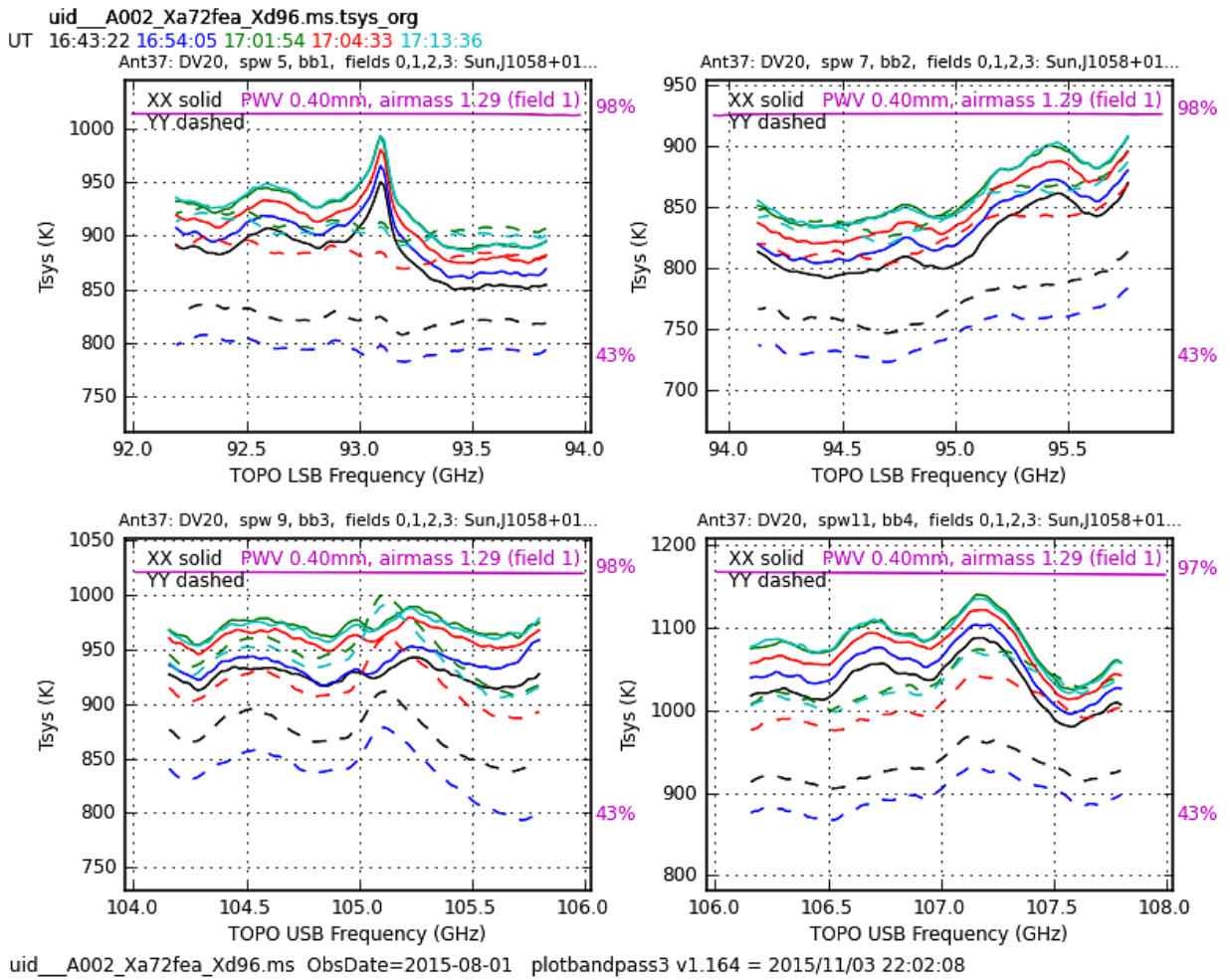
The autocorrelation data output from the correlator cannot be used for these measurements because the correlator has insufficient dynamic range to measure P_{off} . Instead, the measurements rely on the total-power data obtained by the baseband square-law detectors. The antenna temperature of the science target on the Sun is given by:

$$T_{ant} = \frac{(P_{sky} - P_{zero})(P_{sun} - P_{off})}{(P_{off} - P_{zero})(P_{hot} - P_{cold})} (T_{hot} - T_{cold}) \quad (7)$$

The system temperature is given by the ALMA online system.

A typical antenna temperature in solar observing is shown in Figure 11. Upper panel represents MD1 and lower panel MD2 mode measurements, both in Band 3. MD1 mode temperatures are lower due to non-linearity of MD1 mode, as already explained in the previous chapter. Typical values are around 7000 K as expected for this frequency region.

Figure 12 shows system temperatures for DV20 antenna in MD2 mode in Band 3, for all four spectral windows and different polarization products. Typical values are around 900 K which is almost an order of magnitude smaller than the antenna temperature when observing the Sun. Correlated amplitude temperature for the same antenna is shown in Figure 13. Calibrated amplitude of visibility as a function of uv-distance for the same observation is shown in Figure 14.



uid__A002_Xa72fea_Xd96.ms ObsDate=2015-08-01 plotbandpass3 v1.164 = 2015/11/03 22:02:08
Figure 12: T_{sys} of DV20 in band3, MD2, for XX (solid) YY (dashed) polarizations. Different colors indicate different times. (uid://A002/Xa72fea/Xf1e)

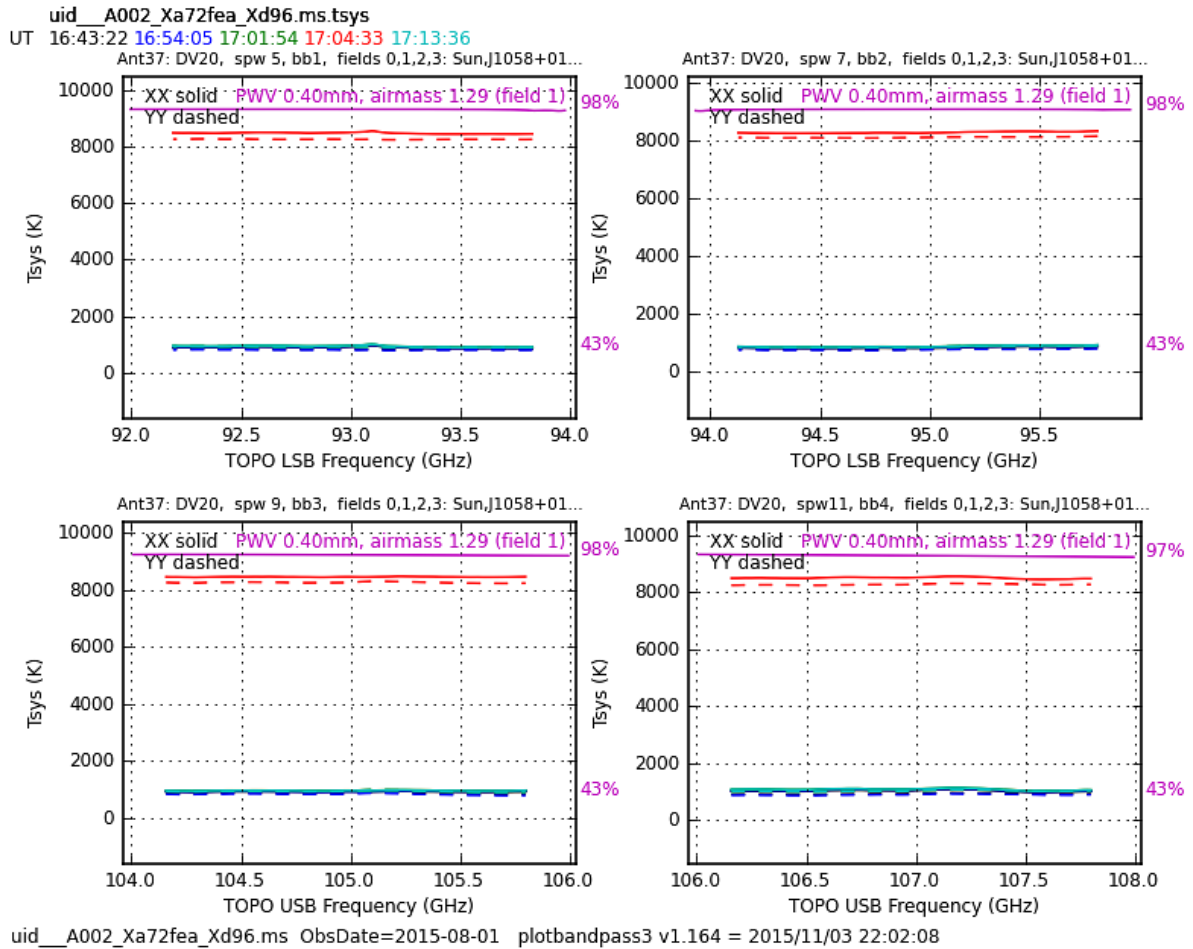


Figure 13: $T_a + T_{sys}$ of DV20 in Band3, MD2, for XX (solid) YY (dashed) polarizations. Different colors indicate different times. (uid://A002/Xa72fea/Xf1e)

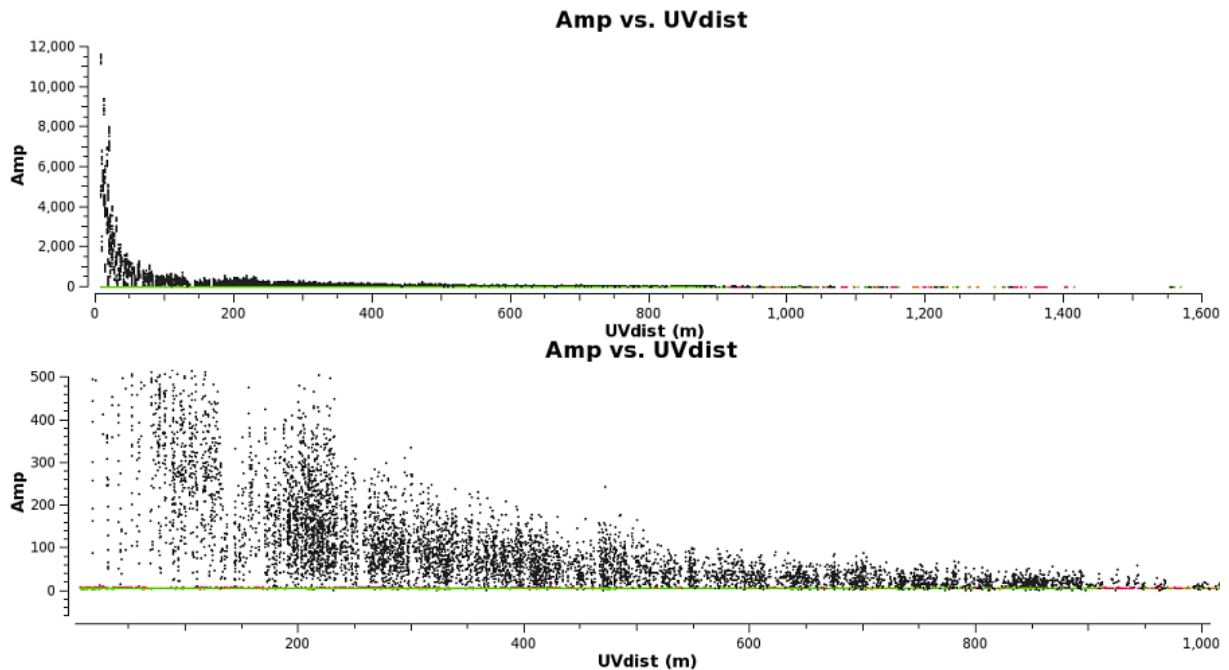


Figure 14: Calibrated amplitude of visibility as a function of the uv-distance. Both panels are made from the same data obtained with Band3-MD2 on 1 August 2015 (uid://A002/Xa72fea/Xf1e). Upper panel: Full range of amplitude, Lower panel: Lower range. Black: Target (Sun), colors: Calibrators.

3.5 Solar Observing Sequence

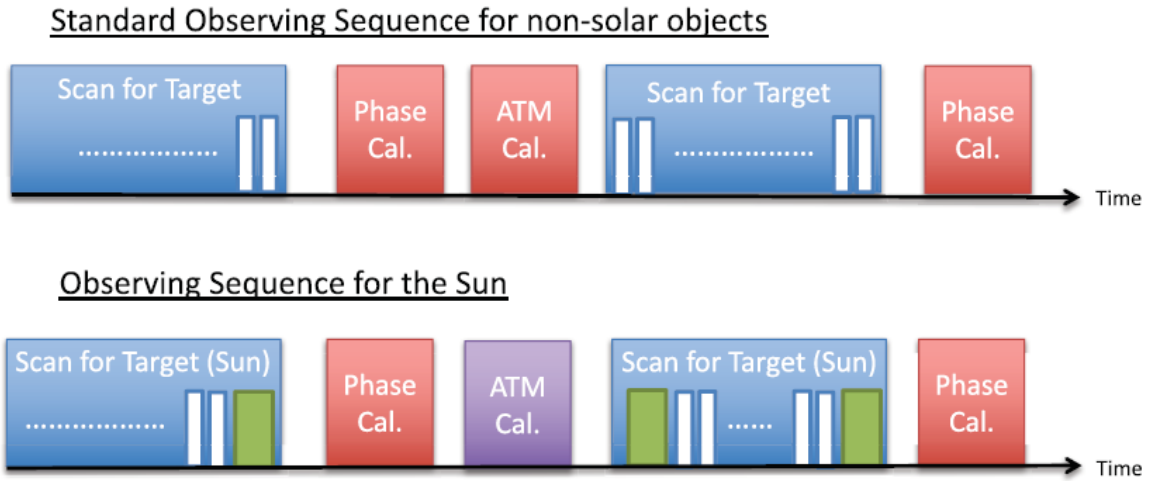


Figure 15: Comparison of the standard observing sequence and the one used in solar observing. Each box indicates a scan which consists of multiple subscans (shown only for target scan). A red box indicates a scan for the phase calibrator; a blue box is the scan for the science target, and a purple box indicates a scan for atmospheric calibration near the target. White narrow boxes indicate subscans of observing the target, and green boxes indicate subscans of observing the sky near the Sun with the attenuating levels adjusted to the Sun (Shimojo et al. 2017).

To derive T_{ant} in practice requires modifying the standard ALMA observing sequence. There are three major differences, as shown schematically in Figure 15. The first is that subscans are needed for observing the sky near the Sun at the start and end of a science-target scan, the reason being that the P_{off} measurement has to be carried out with the attenuator levels set for observing the Sun. Hence, P_{off} is measured by the first and last subscans within the science target scan. The duration of the subscans used for measuring P_{off} is currently set to a few seconds. The second difference from standard procedures is that an atmospheric calibration is not carried out for each calibrator scan because it introduces too long a delay (many minutes) between source scans, to the possible detriment of a given observer's scientific objectives. Instead, the system temperature derived from the atmospheric calibration near the Sun is applied to phase-calibrator data. The third modification is that the measurement of P_{zero} is carried out at the beginning of a solar observation. The value of P_{zero} is found to be very stable for a given antenna and frequency band, so we do not need to carry out the measurement frequently.

3.6 Mosaicking

Considering dynamic solar phenomena with short temporal scales (e.g., quiet Sun waves, flares, etc.), the single pointing interferometric observing is actually desirable because it enables short integration times for high cadence observing. In Cycle 4 this time was limited to 2 seconds, and in Cycle 5 it is lowered to 1 second. We believe that it could be set to even lower values, around 100 msec, limited by the data rate.

However, single pointing of ALMA interferometer results in a very small field of view, 58 arcsec in Band 3 and 26 arcsec in Band 6. Many interesting solar features are much larger

than this, so mosaicking has to be used to observe them, at the expense of cadence. In mosaicking, an image is constructed from a pattern of discrete antenna pointings. Mosaicking has been extensively tested during solar commissioning campaigns and it was shown to work reliably. Figure 16 shows an example of the time variation of T_{ant} for a mosaic observation in MD2 mode in Band 6 for different kind of antennas. It is clear that T_{ant} varies as ALMA antennas point to different locations on the Sun.

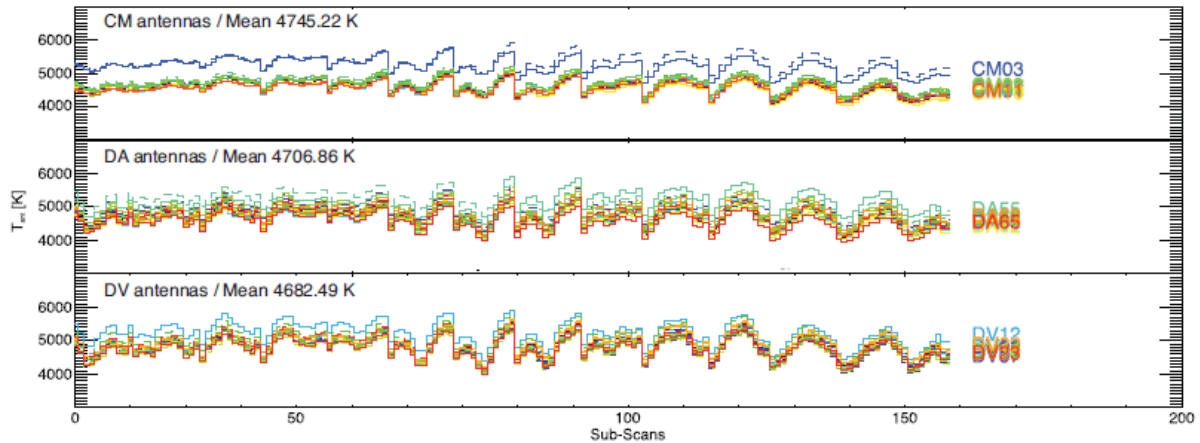


Figure 16: The temporal variation of the antenna temperature as a function of subscan number during the 149-point mosaic observation of a sunspot with Band 6 using the MD2 observing mode. Upper panel: CM antennas, middle panel: DA antennas, lower panel: DV antennas. The polarization is indicated by solid (X) and dashed (Y) lines, while different antennas are denoted by different colours (Shimojo et al. 2017).

3.7 Data and Image Synthesis

When we use the clean task of CASA for synthesizing a solar image, the mosaic option for the imagemode parameter has to be used even for the data of single-pointing observations, to deal with the heterogeneous-array nature of the data. For mosaic observations, the coordinate of each pointing has to be re-calculated relative to the center of the FOV using ALMA pointing data. This is necessary because the heliocentric coordinate frame is moving relative to the RA/Dec coordinate frame during an observation. To improve image quality, the data from all four SPWs for synthesizing one solar image can be used. This is the case with images in this report, so the observing frequency of the solar images shown is the same as the frequency of the first LO: 100 GHz for Band 3, 239 GHz for Band 6.

Figure 17 shows the images of the leading sunspot in AR 12470 on December 16, 2015 synthesized from the 149-point mosaic observation in Band 3. The default visibility weighting option of the CASA clean task is to set the Briggs robust weighting parameter to zero. Artifacts appear in the image in the form of fine stripes, as evident in panels (a) and (c). We attribute this to undue weight being given to longer interferometric baselines. In particular the locations of the centers of 12-m array and 7-m array are not the same; the distance between them is about 200 m. Hence, data on baselines longer than 200 m are always included in solar data, even when the observation is done with the most compact configuration of the 12-m array, as was the case in December 2015. The resulting baseline distribution is non-optimal and the (nonlinear) image deconvolution process is subject to instability. The weighting of these longer baselines can be reduced by applying more natural weighting by setting the

Briggs robust weighting parameter to unity. When this is done, the artificial stripes disappear in the image (panels (b) and (d) of Figure 17). The value is not fully optimized, and the optimal value might depend on the target and array configuration.

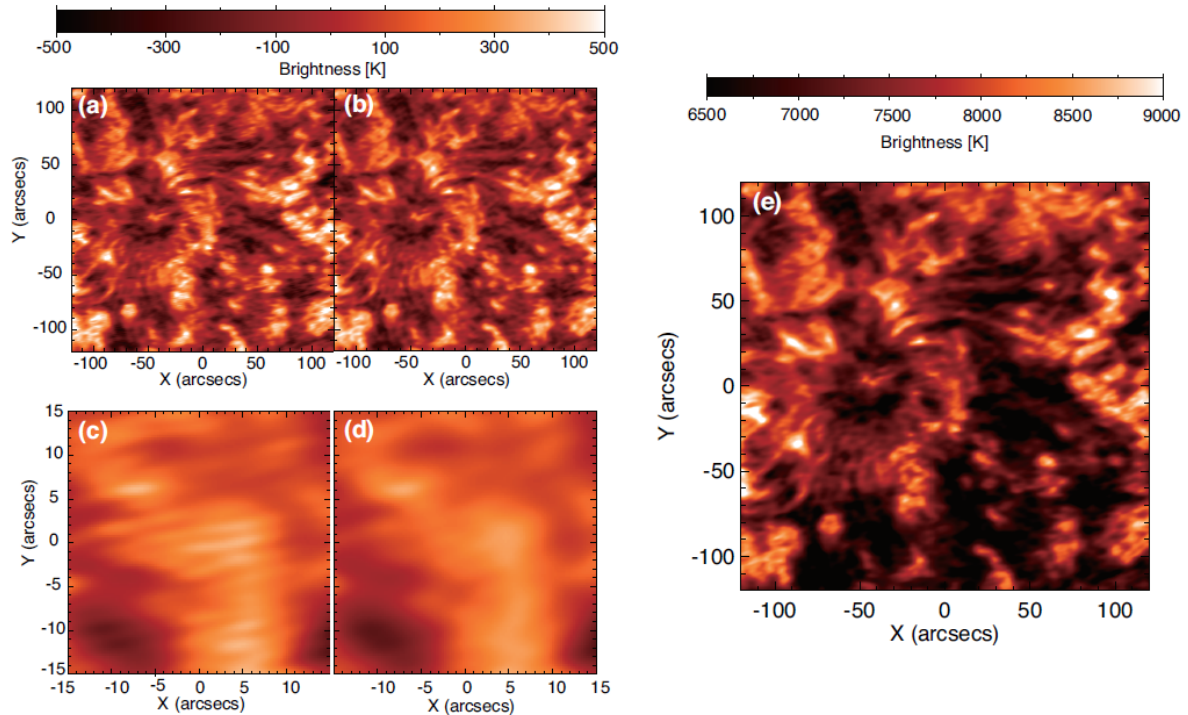


Figure 17: The sunspot images synthesized from a 149-point mosaic observation with Band 3 using the MD2 mode. (a) and (b): Synthesized images of the lead sunspot of AR 12470; (c) and (d): Expanded images around the center of (a) and (b); (e): A combined image created from interferometric and single-dish observations. (a) and (c) are synthesized with a Briggs robust weighting factor $\text{robust}=0.0$ (the CASA default). Images (b), (d), and (e) are synthesized with $\text{robust}=1.0$ (`uid://A002/Xade68e/X180`) (Shimojo et al. 2017).

The synthesized solar images include pixels with negative values. The negative values have physical meaning, because the interferometric data does not include the DC component of the brightness distribution in the field of view. Therefore, simultaneous single-dish observations are essential for obtaining absolute brightness temperatures from ALMA data. Figure 17(e) is the result of combining the synthesized image and the full-disk solar map constructed from the simultaneous single-dish fast-scanning data. A correction factor has been applied to the full disk map created with CASA (see next chapter). For the combination, we use the default parameters of the feather task in CASA. We found that the averaged brightness temperature of the combined image is always larger (5 - 10%) than the temperature brightness at the same position in the single-dish map even though the values should be similar. This means that the parameters of the feather task will need to be tuned in order to obtain consistent images, before using combined images for precise discussion of the absolute brightness temperature.

Figure 18 presents solar images synthesized from a 149-point mosaic observation in Band 6 using the MD2 mode. Panel (a) shows the leading sunspot in AR 12470 on December 18, 2015, and panel (b) shows the solar limb near the south pole on December 20, 2015. The calibration and synthesis imaging process are the same as those employed for Band 3, except for the observing frequency. Note that here the single dish data was not used. The synthesized beams are 2.4×0.9 arcsec for the sunspot image and 1.7×1.0 arcsec for the south pole image.

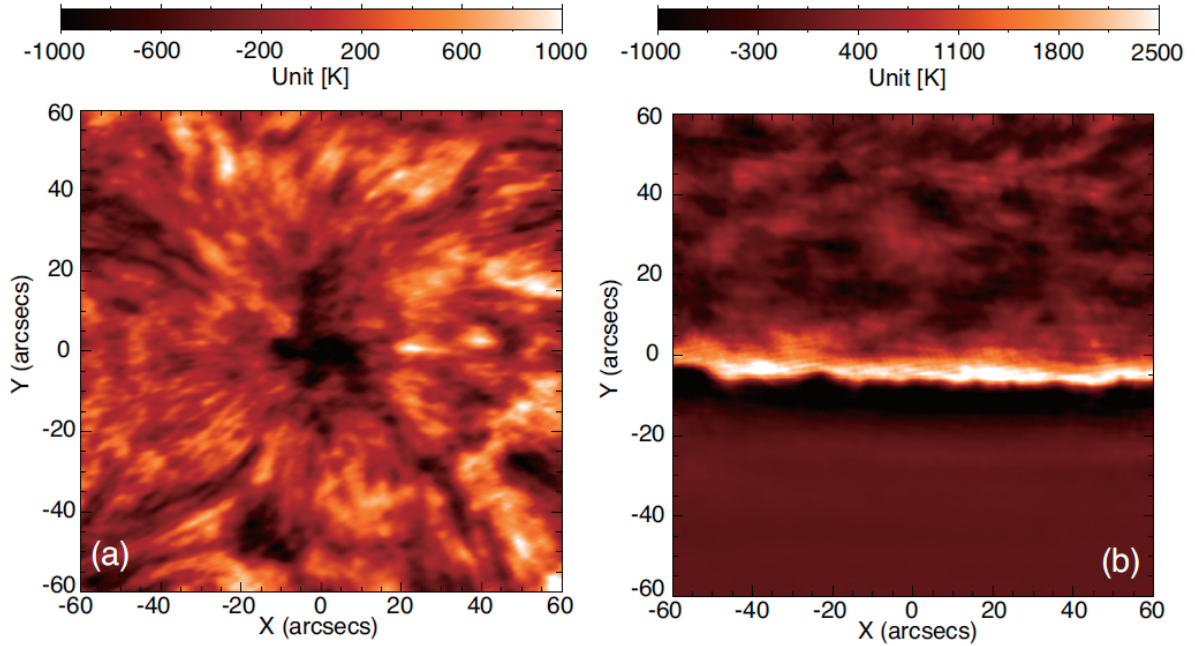


Figure 18: The solar images synthesized from the 149-points mosaic observations with Band 6 using the MD2 mode. (a) The leading sunspot of AR 12470 (uid://A002/Xae00c5/X2a8d), (b) The solar limb around the South Pole (uid://A002/Xae17cd/X367a) (Shimojo et al. 2017).

A narrow bright limb seen in Figure 18(b) is not real, it is rather probably an effect of the high contrast between the solar disk and the sky when observed with an interferometer.

3.8 Noise Level of Solar Images

The noise level of a synthesized image may be determined from the RMS value of the brightness on blank sky. However, this method cannot be applied to solar synthesized images because the primary beam of ALMA antennas is significantly smaller than the Sun in all frequency bands. Solar emission completely fills the field of view in most cases, complicating the task of estimating noise. We therefore use an alternative method based on polarization products (XX, YY) which can be imaged separately from the same observation dataset.

In the absence of any flare emission, solar mm/sub-mm emission is thermal (free-free) emission from optically thick plasma in the solar chromosphere. Although there is possibility that the thermal emission is circularly polarized due to the presence of strong magnetic fields, net linear polarization should be absent due to differential Faraday rotation, and we can assume that any such polarization at 100 GHz and 239 GHz is negligibly small in comparison with the precision of current solar ALMA observations. The crosstalk of the polarizations in the receiver system can be also neglected. Therefore, the difference between the solar images synthesized from XX- and YY- data should be zero in principle, and the difference between the two polarizations can be used as a proxy for the noise level in the final images.

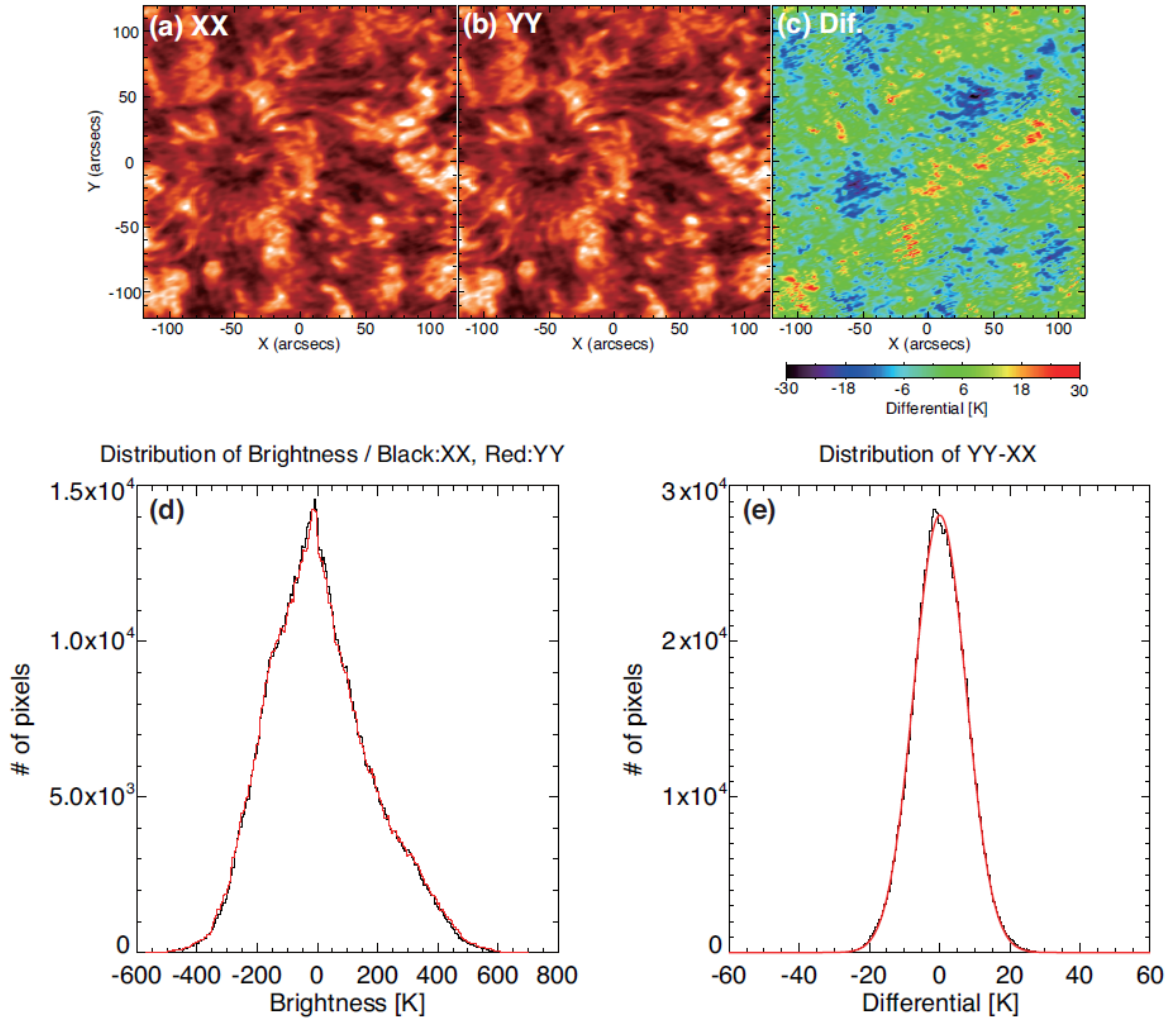


Figure 19: (a) and (b) The Band 3 sunspot images synthesized from the data of XX and YY respectively; (c) The difference image of (a) and (b); (d) The pixel distributions of brightness in (a) [Black] and (b) [Red]; (e) the pixel distribution function of the difference image (c). The red line on (e) indicates the Gaussian function fit to the distribution (Shimojo et al. 2017).

Figure 19 shows estimations of the noise-level from maps formed using the XX- and YY- correlations. From the width of the Gaussian function fitted to the distribution of the differential, the noise level of the Band 3 synthesized image of the sunspot (Figure 17 (b)) is 3.7 K when the integration time is 6 seconds and the integration bandwidth is 8 GHz. We also apply the method to the sunspot image observed with Band 6 (Figure 18(a)), and estimate the noise level to be 9.8 K. The integration time and bandwidth of the Band 6 image are the same as those of the Band 3 image.

3.9 Imaging Artifacts Above the Solar Limb

In addition to thermal noise, imaging artifacts may be present in a synthesis image as a result of incomplete sampling of the uv-plane, non-optimum weighting of the visibility data, source variability, or other factors. An example of an artifact resulting from incomplete sampling and possibly non-optimum weighting is shown in Figure 20, in which a detail of the mosaic image of the South Pole is shown. Figure (a) shows a map made using the heterogeneous array comprised of 7 m antennas and 12 m antennas, (b) shows the same image using only the 12 m antennas and (c) shows the same image using only the 7 m antennas. A stripe of negative flux density appears above the limb in (a) and a stripe of positive flux density is seen even higher above the limb. The stripes are non-physical artifacts due to what we believe incomplete sampling of the high contrast represented by the bright solar disk falling off to cold sky. The interferometric array shows ringing or overshoot response as a result.

In the image synthesized from only 7 m antennas the positive enhancement is very weak (blue lines in (d) and (e)) although the negative stripe persists. The image synthesized from only 12 m antennas shows a stronger enhancement with a peak located about 20 arcsec above the limb (red lines). We note that the shortest baseline of the 12-m array observing the solar limb is 12.9 m, so the largest angular scale measured is 20.1 arcsec at 239 GHz. For the heterogeneous array the shortest baseline measured is 7.6 m, corresponding to an angular scale of 34.3 arcsec. In principle, inclusion of the 7 m antennas should bridge the gap between the single-dish total-power map (resolution 24.4 arcsec) and the largest angular scale measured by the 12-m array.

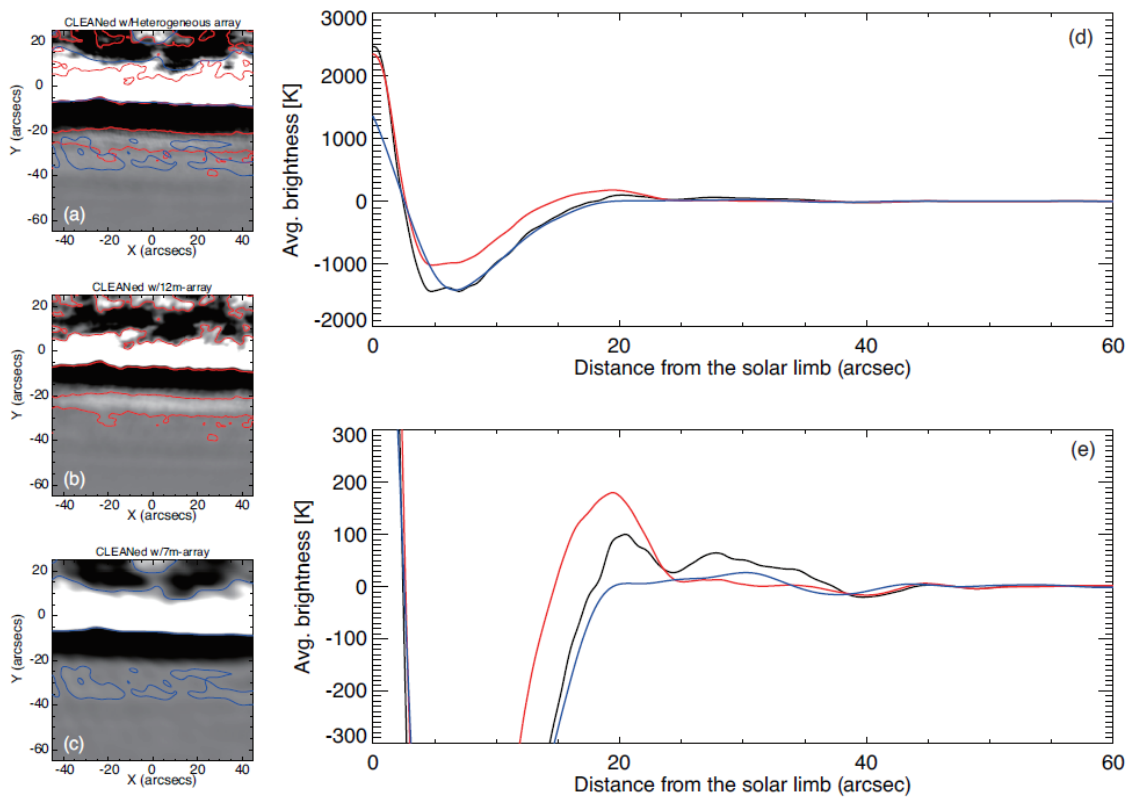


Figure 20: The solar-limb images synthesized from the data of the (a) heterogeneous array, (b) 12-m array, and (c) 7-m array. The red and blue contours in the panels indicate +20 K level of 12-m array and 7-m array respectively. (d) and (e) show the brightness profiles as a function of the distance from the solar limb. Black: heterogeneous array, Red: 12-m array, Blue: 7-m array. The difference of (d) and (e) is the range of the y-axis. (Shimojo et al. 2017).

A possibility is that the relative weighting of the visibility baselines is incorrect: a careful assessment of the weights assigned to 7 m - 7 m, 7 m - 12 m, and 12 m - 12 m baselines, as well as the weight given to the single dish total power map is needed. A final possibility is insufficient numbers of short antenna baselines. The 7-m array provides short baselines, and the visibilities of the baselines should suppress the sidelobes created by the 12-m array. In our case, we can see the suppression of the sidelobe by 7 m antennas (see the difference of the red and black lines in Figure 20). The remaining enhancement in the image synthesized from the data with the 7 m + 12 m heterogeneous array might indicate the lack of the short baselines.

3.10 Co-alignment between ALMA and other instruments

To maximize the scientific impact of ALMA data, it is very important to compare ALMA images with those obtained by instruments operating at other wavelengths with similar angular resolution. Direct comparisons require that ALMA images are accurately co-aligned with those produced by other telescopes. ALMA operates in a geocentric coordinate frame using celestial equatorial system while heliocentric coordinates are usually used for solar imaging data. Therefore, ALMA images must be converted from RA/Dec coordinates to a heliocentric coordinate frame. A method for this is described in the next chapter.

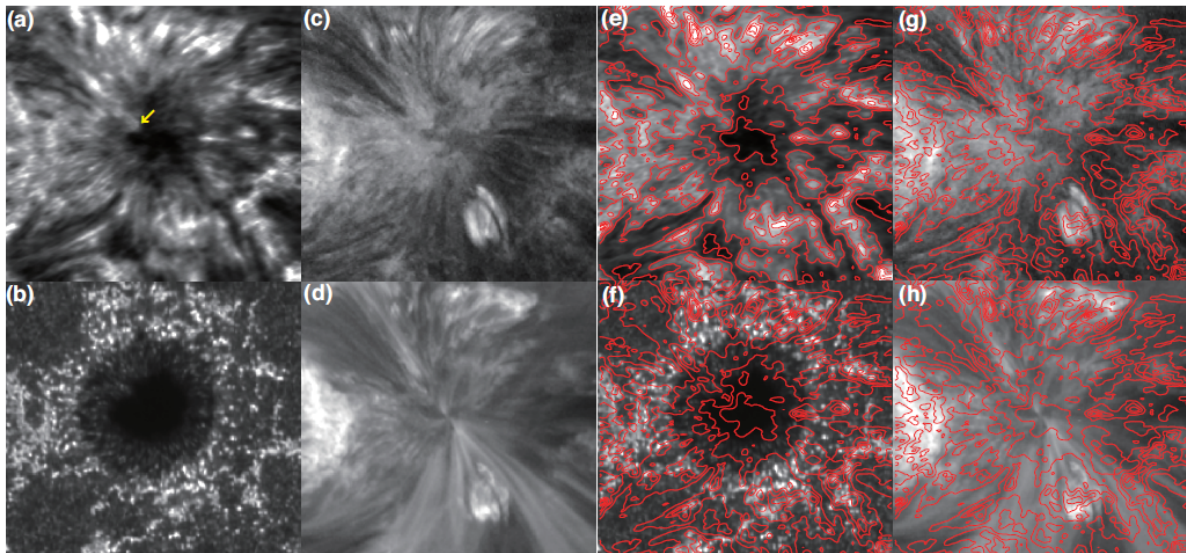


Figure 21: Co-alignment between the ALMA Band 6 image and SDO/AIA images. The gray scale: (a) and (e): ALMA Band 6 synthesized image with the feathering process, (b) and (f) 170 nm band of SDO/AIA, (c) & (g) 30.4 nm band of SDO/AIA, (d) and (h) 19.3 nm band of SDO/AIA. The red contours on (e), (f), (g), and (h) indicate the brightness of the ALMA Band 6 image (a). (Shimojo et al. 2017)

The precision of the absolute pointing of the ALMA antennas is better than 2 arcsec. Figure 21 shows the result of co-alignment between the ALMA Band 6 sunspot image with UV continuum, and EUV images obtained with Solar Dynamics Observatory/Atmospheric Imaging Assembly (SDO/AIA). For the co-alignments, we do not make any adjustment except for the coordinate conversion. The bright structure above the remnant of the light bridge in the AIA 30.4 nm image is very similar to that in the ALMA Band 6 image. In comparing the edge of the structure in the umbra (yellow arrow in Figure 21a) the precision of the co-alignment appears to be better than the size of the synthesized beam.

Similarly, Figure 22 shows the result of the co-alignment between the ALMA Band 6 image and the Mg ii k2v image obtained with the Interface Region Imaging Spectrograph (IRIS). In this case, we can easily identify the counterparts of the Band 6 image in the IRIS image. The similarity between the images suggests that Band 6 and Mg ii k2v line emissions are formed within approximately the same range of heights.

In Figure 23, the ALMA Band 3 mosaic is compared to SDO/AIA 170 nm, 19.3 nm and 30.4 nm channels, SDO/HMI magnetogram and ground-based H α wing image retrieved from SOLIS/FDP archive (Brajša et al. 2017b). Small bright structures, marked with blue rectangles in the ALMA image, appear bright in the SDO/AIA 170 nm channel and dark in H α wing image. The same features can be identified in magnetogram as magnetic bipoles. Large structures (red rectangles) are also visible in SDO/AIA 30.4 nm and 19.3 nm channels. It is interesting to note that streaks that seem to radiate from the sunspot in the ALMA image correspond well to AIA 30.4 nm image. Moreover, the H α wing image looks like inverted ALMA image. All this leads to conclusion that ALMA interferometric imaging is working very well and that the image overlapping is performed correctly.

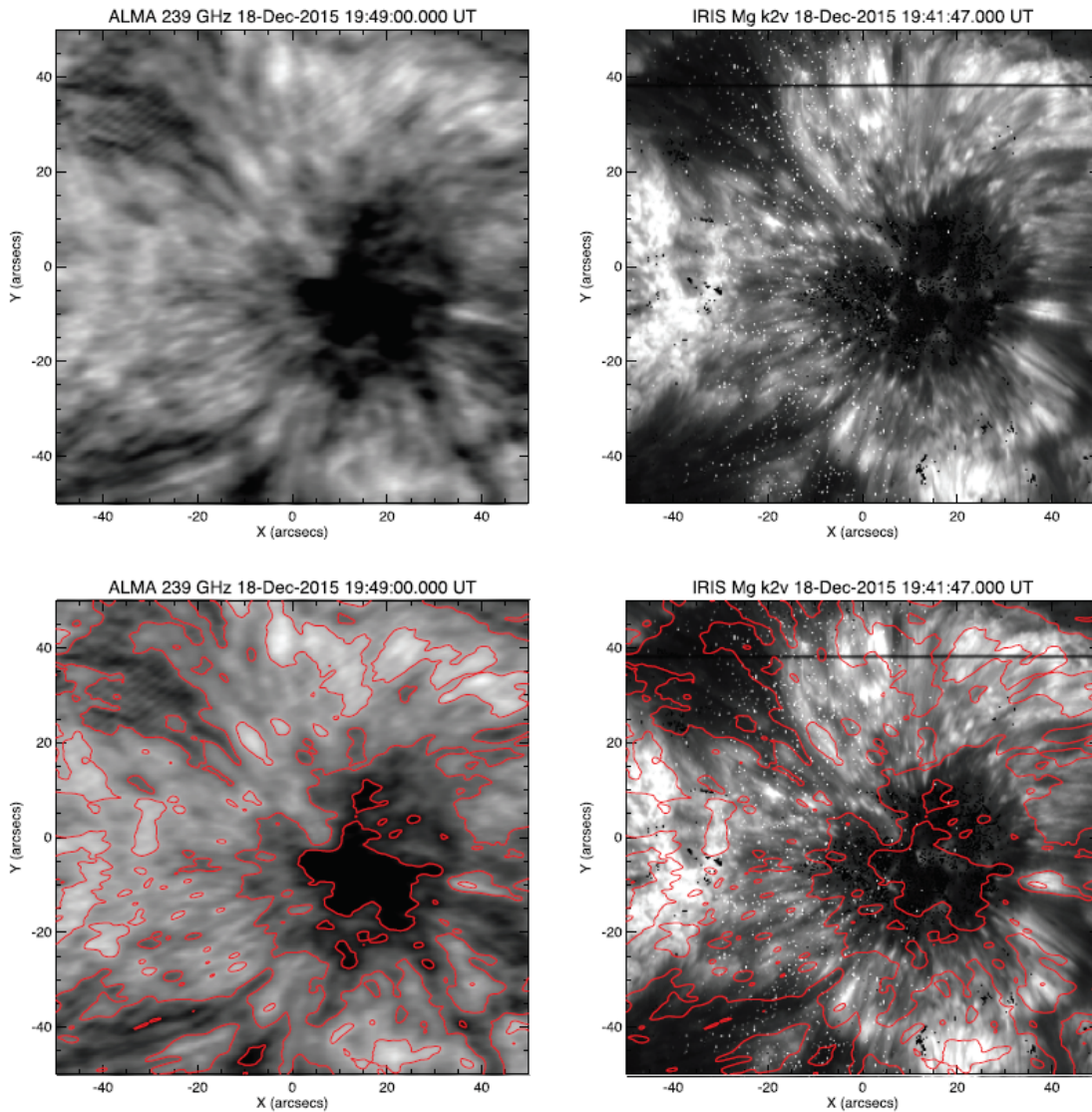


Figure 22: Co-alignment between the ALMA Band 6 image and Mg k2v line image obtained with IRIS. Left: ALMA 239 GHz images. Right: Mg k2v image. Red contours indicate the brightness of the ALMA image. (Shimojo et al. 2017).

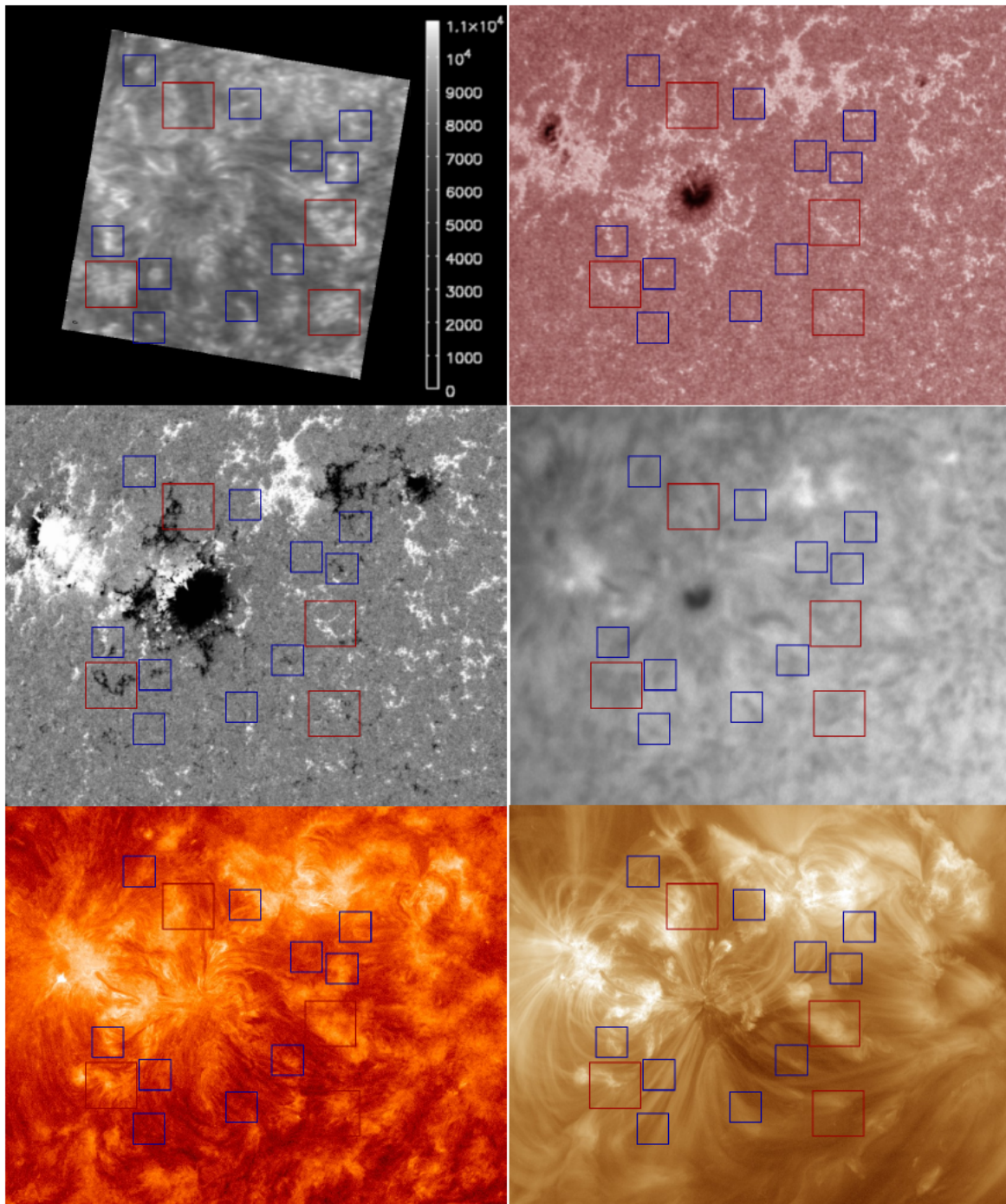


Figure 23: Active region AR 12470 observed with ALMA in Band 3 using 149-pt mosaic (upper left panel) compared to SDO/AIA 170 nm channel (upper right), SDO/HMI magnetogram (middle left), H α wing line from SOLIS/FDP (middle right) and SDO/AIA 30.4 nm (lower left) and 19.3 nm (lower right) channels (uid://A002/Xade68e/X180). (Brajša et al., 2017b).

4 SINGLE-DISH SOLAR OBSERVING

The field of view of both 7-meter and 12-meter ALMA antennas is much smaller than the apparent angular diameter of the Sun which makes the ALMA interferometer insensitive to solar background emission since large spatial scales are resolved out. Measurement of the absolute brightness temperature of the Sun, and its variation with frequency which corresponds to different heights in the solar atmosphere, is essential for much of the ALMA solar science. Single-dish data taken simultaneously with interferometric observation can restore information on the absolute temperature scale missing from the interferometer data and also recover the large spatial scales in interferometric mosaic images. Even the standalone single-dish data is extremely useful for studies of the Sun because it can cover wider areas than interferometer mosaicking is able to do, and in much shorter time. This enables observations of larger-scale phenomena with much better time cadence, although at a lower spatial resolution. Moreover, full-disk solar images are useful for studies of limb brightening and for distinguishing between various solar atmospheric models.

In summary, single-dish observing is needed for:

- measurement of absolute brightness temperature,
- recovery of the large spatial scales,
- fast mapping of wider areas,
- obtaining full-disc maps of the Sun.

4.1 Fast-scan Mapping

Fast-scanning mapping techniques were first developed in a non-solar context by R. Hills and N. Phillips during commissioning campaigns in 2010-2014 (summarized under CSV-239) and later applied to solar observing (December 2014/2015 campaigns, CSV-3162/3244). In December 2015 extensive tests were carried out in order to optimize the fast-scanning procedure for the first regular solar observations which started in 2016 within Cycle 4.

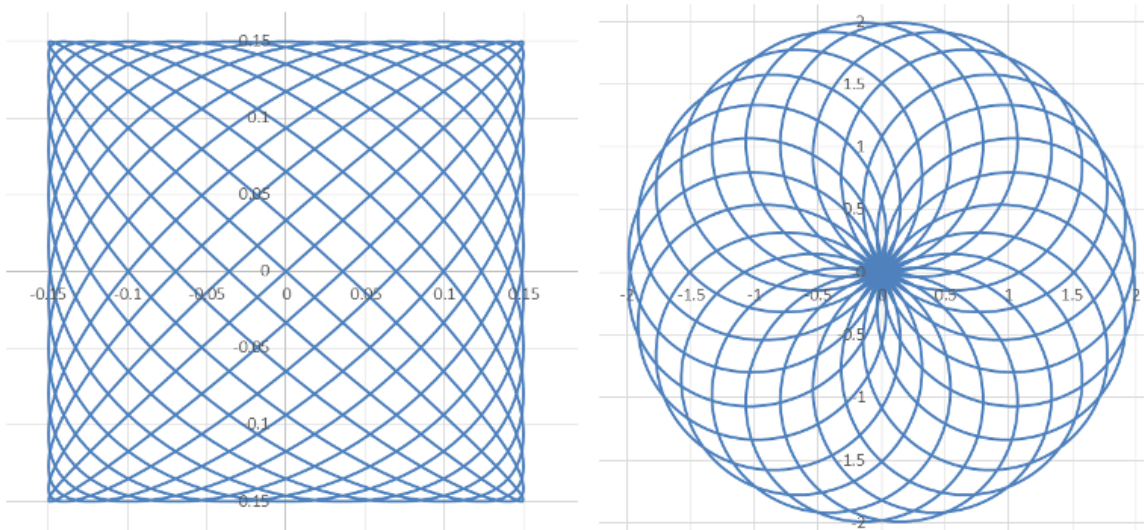


Figure 24: Single-dish fast-scanning patterns. Lissajous pattern (left) can be used for mapping rectangular regions while double-circle pattern (right) can be used for mapping circular regions or the whole solar disk.

In principle, fast-scanning entails a continuous movement of the antenna across the target region using a mapping pattern which minimizes sudden acceleration of the drive motors. Two mapping techniques were developed and tested, using either Lissajous or double-circle patterns (Figure 24). Lissajous pattern is appropriate for mapping smaller rectangular regions, while double-circle pattern is mostly used for full-disk mapping. A major advantage of fast-scanning is that it minimizes the variation of atmospheric opacity by repeatedly observing the same region. Another advantage is the speed – whole disk maps can be made in only several minutes and can be used to study the time-varying phenomena.

Commissioning work has focused on PM antennas because it is expected that those antennas will be used for single-dish mapping during regular operations (as has been the case in Cycle 4). For a successful mapping, a servo characterization of the antennas was carried out by comparing the commanded and reported antenna positions under a range of conditions (Hills, PM Antenna Servo Characterization 2016).

4.1.1 Lissajous Mapping

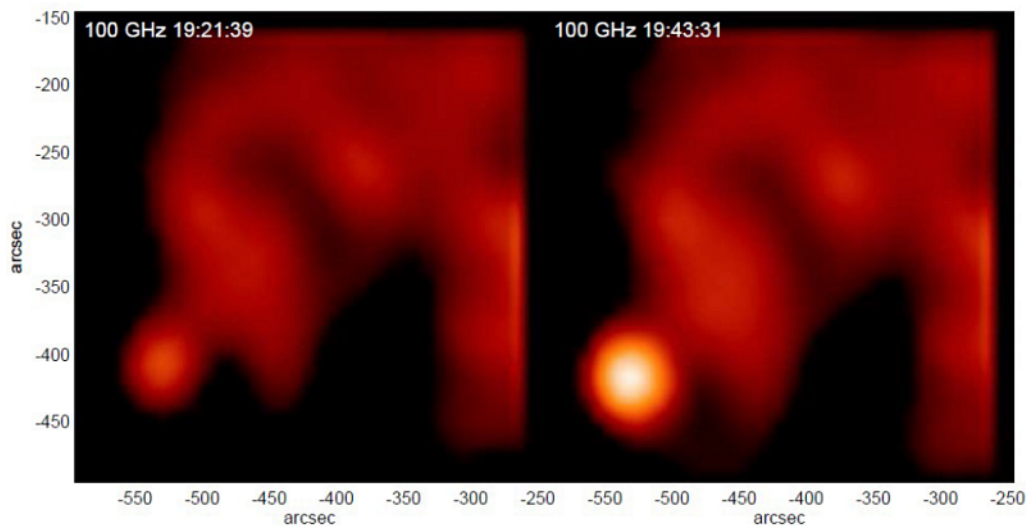


Figure 25: A solar flare observed on December 14, 2014 in Band 3 using Lissajous fast-scanning pattern of a region 6 x 6 arcmin. Each image took about 30 seconds to complete with the PM01 antenna.

Lissajous pattern is suitable for fast-scanning rectangular regions on the Sun. The pattern is not as smooth as double-circle and there are variations in antenna slew speed and acceleration. During the December 2014 campaign, a test mapping by using fast-scanning Lissajous patterns of smaller regions of the Sun was performed. Luckily, a small flare occurred in the region being mapped, and it was possible to follow its brightening (Figure 25). This observation was made with the PM01 with the bad sub-reflector so that the effective beam size is larger than it should be.

This observation demonstrated that the PM antennas are able to map regions on the solar disk of scientific interest with a cadence of 30 seconds, which is adequate for some flare science and for chromospheric oscillation studies (dominant periods of 180-300 s).

4.1.2 Double-circle Fast-scanning

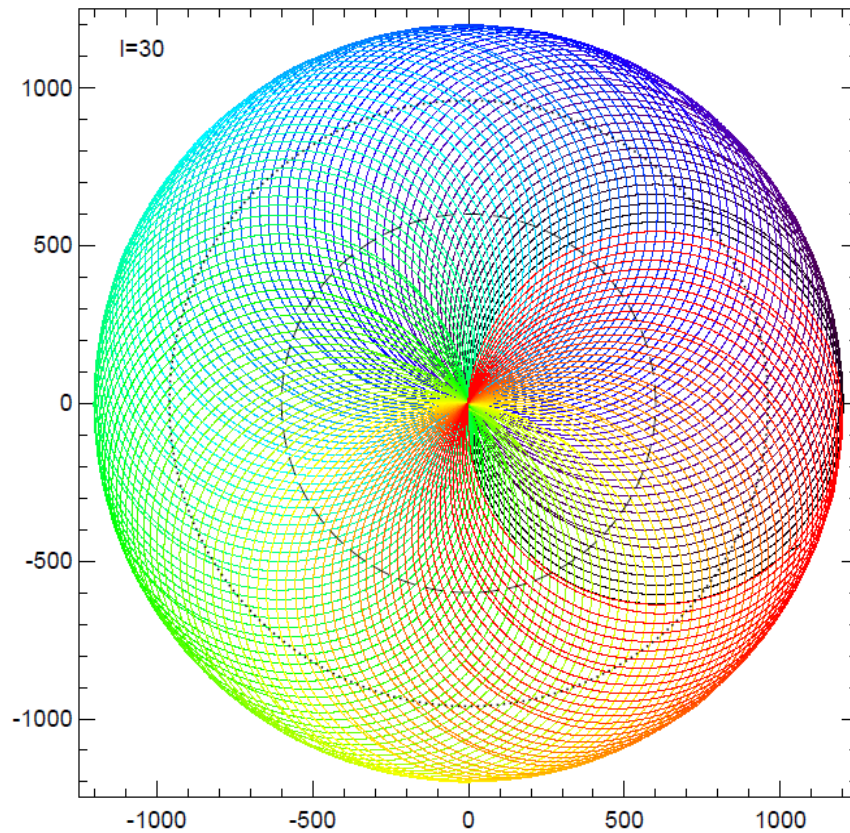


Figure 26: Double-circle single-dish scanning pattern. Consecutive minor circles which denote the actual path of the antenna are coloured. Inner dashed circle denotes the major circle around which minor circles move. Dotted circle represents the solar disk. Units are given in arcseconds. (White et al. 2017)

In the double-circle pattern, the antenna scans the target following a circular trajectory (minor circle) whose center moves around on another (major) circle which is centered on the target (Figure 26). An advantage of this type of mapping is that antenna moves steadily with constant velocity throughout the target and there are no sharp turns or accelerations. For solar full-disk mapping, radius of the minor and major circle are fixed at 600 arcsec which results in a circular field of view of 2400 arcsec in diameter. This is ~ 400 arcsec larger than the apparent diameter of the Sun in order to enable imaging of the solar prominences on the limb and also to include blank-sky measurements for calibration checks.

The script used for the single-dish fast scanning, *FastScanObs_md.py*, has several parameters which can be adjusted for optimal mapping. The number of minor circles in a pattern is controlled by *samplingLength* (l) parameter (Figure 27) which defines the spacing of the centers of the minor circles as they move around the major circle. The duration of the complete scan of the target is controlled by *subscanDuration* parameter which is selected in a way that the whole target is mapped once, and it depends on the *samplingLength*. Different values of the *samplingLength* parameter were tested and for each the duration of the scans to obtain a full map was measured. The results are listed in Table 6. Due to safety limitations of the antenna drive in maximum permitted velocity (1 deg/sec) and acceleration (3 deg/sec²),

which are taken into account in the software, the scan duration does not linearly depend on the *samplingLength*.

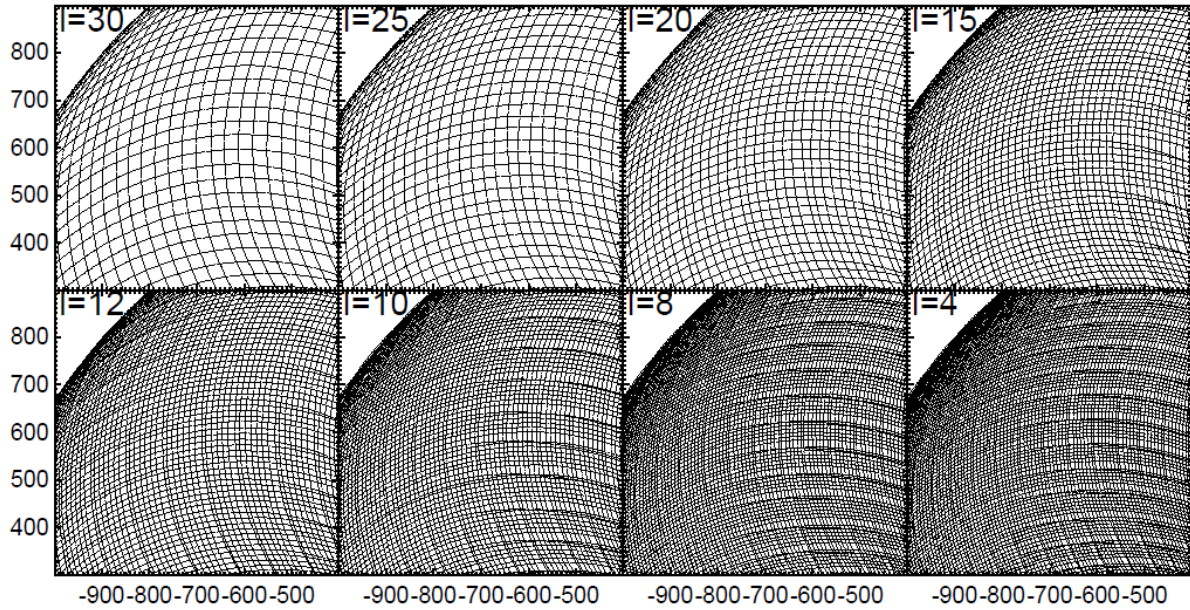


Figure 27: Close-up of the actual double-circle pattern for several different values of *samplingLength* parameter (*l*). Each 1 millisecond sample is plotted as one dot. (White et al. 2017)

The actual mapping pattern is slightly irregular and the exact cause of this is still under investigation. However, the size of irregularities is very small and does not affect the final map since the target is over-sampled and the data points are regridded onto a rectangular mesh according to their actual measured positions.

Table 6: Whole Sun scan durations for different values of the *samplingLength* parameter. (White et al. 2017)

<i>samplingLength</i> (arcsec)	30	25	20	15	12	10	8	4
Scan duration (seconds)	187	224	280	373	467	560	701	1397
Minor circles per pattern	125	150	188	251	314	377	471	943

The optimal choice of the *samplingLength* value is a trade-off between adequate sampling of the target and the duration of the scan. For Bands 3 and 6, the Nyquist limit requires sampling distances of at most 30 arcsec and 12 arcsec, respectively. To deduce the optimal *samplingLength* value, a test of image quality was performed (Iwai, 2016), where a model solar image was convolved with the telescope response and sampled using a double-circle pattern with different *samplingLength* values. The result was imaged using a triangulation gridding method. A torus just inside the limb was compared for various *samplingLength* values and the correlation coefficient was computed for a reference *samplingLength* value of 4 arcsec. The results show a decline in the correlation coefficient beyond 20 arcsec in Band 3 and 12 arcsec in Band 6 (Figure 28). The final values used for fast scanning are 20 arcsec in Band 3 and 10 arcsec in Band 6, which correspond to 13 and 17 minutes of total observation time including all calibrations.

The quality of the final image also depends on the sampling interval. The ALMA total power detectors have a hardware sampling rate of 0.5 milliseconds, while fast-scanning tests were usually performed with 1-2 millisecond rate. Such a short rate is possible because the Sun is so bright that it dominates the signal even at that temporal resolution. For the current solar single-dish observations, the sampling time used is 1 millisecond which results in a spatial

distance of about 2.5 arcsec on the sky. This is well below the Nyquist limit but such short integrations are valuable for providing flexibility in removing any bad measurements. With this rate, each minor circle takes about 1.5 seconds.

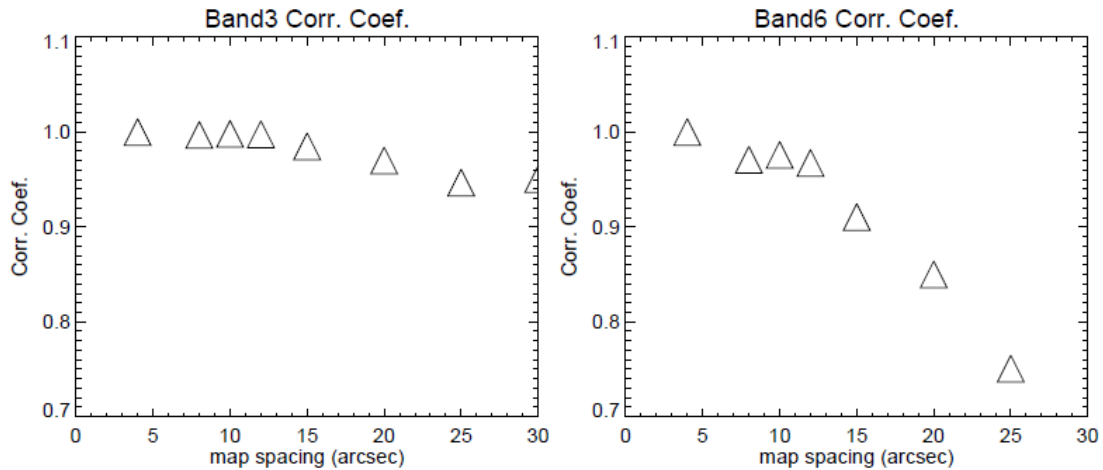


Figure 28: Correlation coefficient of intensity as a function of the *samplingLength* parameter for Bands 3 and 6. (White et al. 2017)

The telescope pointing information coming from the drive software is sampled at a much slower rate of 48 milliseconds. The mapping software has to interpolate this pointing data onto the 1 millisecond timescale of the total power samples. Care has to be taken since the interpolation is not linear; it should rather follow a curved telescope path on the sky.

The samples taken during fast-scanning are irregularly placed at points corresponding to actual antenna locations. During imaging process, those samples are gridded onto a regular grid. Two gridding functions are usually used in ALMA single-dish imaging, a spheroidal function and a "GJinc" function. Both are implemented in the CASA software. Although GJinc can give slightly better spatial resolution, spheroidal function gridding is recommended as the standard method for ALMA (Brogan and Hunter, 2014). Processed double-circle fast-scan images can still show trace artefacts of the scanning pattern, especially at the limb where the contrast is high. These result from errors in the assumed pointing of the antenna and/or the timing of the samples.

Antenna velocity and acceleration safety limits, which were already mentioned, also impose limits on the allowed elevation of the target. The reasons for this are azimuthal antenna mounts in which a drive needs to cover a larger angular distance for the same size of the patch of the sky at higher elevations. The elevation limit is set to 70 degrees since the fast scanning already drives antennas close to their limits. The limit for interferometric observing is more relaxed and is set at 82 degrees because the antennas only need to follow one point on the sky.

4.2 Calibration Strategy

The single-dish measurements provide the (background) absolute brightness temperature scale which is missing from the interferometric data. Therefore, the calibration of single-dish data is an extremely important part of the ALMA solar observing. The standard calibration method involves measurement of some reference sources with a well-known flux, such as a quasar, a planet or a reference load. The problem with solar observing calibration is the high system temperature and the lack of bright reference sources, especially those which would fill

the beam of the antenna like the Sun does. The Moon can be used for this purpose, but it is only occasionally located near the Sun and the difference in the brightness temperature is significant. Currently, a "dual-load" calibration method is used for solar observing, which is a modified version of the standard ALMA single-dish calibration method.

The ALMA antennas are equipped with the ALMA Calibration Devices (ACDs) which consist of two microwave absorbers at different temperatures (ambient and hot, at 20° and 85° C, respectively) which can be placed into the optical path of the receiver. A dual-load calibration method relies on the measurements of the received power when these absorbers are placed into the antenna beam, as well as on measurements when antenna is pointed on and off the target source.

The standard method for calibration depends on measuring the system temperature T_{sys} (total thermal noise level in the system excluding the target source) and applying it to the power measurements:

$$T_{src} = T_{sys} \frac{P_{src} - P_{ref}}{P_{ref}} \quad (8)$$

where P_{src} is the power measured when pointing at the target, while P_{ref} is the power measured at a reference position with the corresponding temperature T_{sys} (no target source power). In a dual-load calibration method, 5 second measurements of the receiver power are made at the beginning and end of each single-dish scan for the following targets (P denotes median measured power and T is the temperature):

- a “zero” level measurement, P_{zero} , which reports the levels in the detectors when no power is being supplied. In the ALMA case, the zero levels are very stable over many days for a given antenna and a receiver. Usually, P_{zero} has much smaller values than other measured powers and can be neglected. But in the solar case, the P_{off} measurement (see below) can have comparable values because of the high attenuation used when observing the Sun, and neglecting P_{zero} leads to errors larger than 10%. Note that P_{zero} is only relevant for total power detectors, not for correlation data.
- a “sky” observation offset typically 2° from the target but at the same elevation. This measured power can be expressed as:

$$P_{sky} = G \{ T_{rec} + (1 - e^{-\tau}) \eta_1 T_{atm} + (1 - \eta_1) T_{spill} + e^{-\tau} \eta_1 T_{CMB} \} + P_{zero} \quad (9)$$

G is the receiver gain, T_{rec} is the intrinsic thermal noise of the receiver, η_1 is the antenna efficiency for a source that is much larger than the primary beam, T_{atm} is the equivalent temperature of the atmosphere that contributes most to the emission, τ is the opacity of the atmosphere (for a given telescope elevation h , τ is the zenith opacity τ_0 times the “air mass” $1/\sin(h)$). Above the atmosphere, the sky is filled by the cosmic microwave background (CMB). This must pass through the atmosphere and hence is attenuated by a factor $e^{-\tau}$ when it reaches the telescope. η_1 is referred to as the forward efficiency, which is a product of efficiency η_r that accounts for ohmic losses and the rear spillover efficiency η_{rss} that accounts for the signal that is reflected off the subreflector or other surface above the dish, but not coming from the main dish. The effective temperature of this contribution, T_{spill} , is usually at the ambient temperature of the telescope.

- an “ambient” load observation in which an absorber at the temperature of the thermally–controlled receiver cabin (nominally 20° C) fills the beam path:

$$P_{amb} = G(T_{rec} + T_{amb}) + P_{zero} \quad (10)$$

- a “hot” load observation in which an absorber heated to 70° C fills the beam path:

$$P_{hot} = G(T_{rec} + T_{hot}) + P_{zero} \quad (11)$$

- measurements on the source, made after setting the IF attenuation to get appropriate power levels (resulting in different gain, G_{src}):

$$P_{src} = G_{src} \{ T_{rec} + e^{-\tau} \eta_1 T_{src}^* + (1 - e^{-\tau}) \eta_1 T_{atm} + (1 - \eta_1) T_{spill} + e^{-\tau} \eta_1 T_{CMB} \} + P_{zero} \quad (12)$$

- and an “off” measurement, offset from the source like the initial sky measurement, but made with the same IF attenuation setting as the source data and therefore with the same gain:

$$P_{off} = G_{src} \{ T_{rec} + (1 - e^{-\tau}) \eta_1 T_{atm} + (1 - \eta_1) T_{spill} + e^{-\tau} \eta_1 T_{CMB} \} + P_{zero} \quad (13)$$

Solving for the receiver temperature gives:

$$T_{rec} = \frac{T_{hot}(P_{amb} - P_{zero}) - T_{amb}(P_{hot} - P_{zero})}{P_{hot} - P_{amb}} \quad (14)$$

and for the sky temperature contribution:

$$T_{sky} = \frac{(P_{sky} - P_{zero})(T_{hot} - T_{amb})}{P_{hot} - P_{amb}} - T_{rec} \quad (15)$$

Usually, $T_{sys} = T_{rec} + T_{sky}$, but ALMA on-line calibration system reports values corrected for the atmosphere and forward efficiency, so we do the same:

$$T_{sys} = \frac{(P_{sky} - P_{zero})(T_{hot} - T_{amb})}{\eta_1 e^{-\tau} (P_{hot} - P_{amb})} \quad (16)$$

Neglecting the CMB contribution (~1 K compared to the system temperature of ~1000 K in MD2 mode), the source brightness temperature is:

$$T_{src}^* = \frac{(P_{sky} - P_{zero})(P_{src} - P_{off})(T_{hot} - T_{amb})}{\eta_1 e^{-\tau} (P_{hot} - P_{amb})(P_{off} - P_{zero})} \quad (17)$$

This source temperature still includes contribution of the signal coming to the receiver from outside the subreflector which is usually represented as forward scattering and spillover

efficiency, η_{fss} . To derive the actual brightness temperature of the Sun, T_{src} , which would be seen by a perfect telescope above the atmosphere, the last result needs to be divided by η_{fss} :

$$T_{src} = \frac{(P_{sky} - P_{zero})(P_{src} - P_{off})(T_{hot} - T_{amb})}{\eta_1 \eta_{fss} e^{-\tau} (P_{hot} - P_{amb})(P_{off} - P_{zero})} \quad (18)$$

Efficiencies η_l and η_{fss} are not well measured quantities for the ALMA antennas. This is not relevant for calibration of interferometric data because in that case amplitudes are scaled to astronomical calibrators. Single-dish observations using normal mixer mode and full sensitivity can also be scaled to bright calibrators such as planets. For the solar mode, the Moon can be used as a calibrator without the knowledge of the antenna parameters. However, this is a significant undertaking.

But, for a dual-calibration method used here, those efficiencies are essential. TELCAL package of ALMA uses a fixed value of $\eta_l=0.98$ in all bands. Different wavelengths have different scattering properties for the same antenna so it is unlikely that this efficiency stays the same in all bands. Estimations of η_l using sky-dip measurements give average values for the PM antennas of 0.94 at Band 3 and 0.92 at Band 6, with systematic uncertainties of at least 5% (Tamura and Sugimoto, 2012). In the absence of better data, an average value of the measured and TELCAL efficiencies is used (the first column in Table 7), which roughly corresponds to the technical requirements of ALMA ($\eta_l > 0.95$).

Table 7: Antenna efficiencies used for solar calibration. The last column gives the correction factor $0.98/\eta_l/\eta_{fss}$ to be applied to single-dish solar images produced by standard processing in CASA, which assumes $\eta_l=0.98$ and does not correct for η_{fss} . (White et al. 2017)

	Forward efficiency (η_l)	Forward scattering and spillover (η_{fss})	CASA correction factor
Band 3	0.96 ± 0.02	0.91 ± 0.03	1.12
Band 6	0.95 ± 0.03	0.89 ± 0.03	1.16

Forward scattering and spillover efficiency is estimated at ~ 0.9 (second column in Table 7), based on forward spillover measurements carried out during commissioning and on additional blockage and scattering by the subreflector and its support.

The ALMA TELCAL component uses atmospheric calibrations carried out at the beginning and the end of each fast-scanning observation to calculate the system temperature and atmospheric opacity. These values are available in the final dataset. A correction factor (listed in the last column in Table 7) is needed when CASA is used to calibrate single-dish data because TELCAL assumes a fixed value for $\eta_l=0.98$, and does not correct for η_{fss} . This can be done using an "immath" task after the imaging step, or during calibration in a "gencal" task. In the latter case, the value supplied is the inverse square root of the correction factor, since gains refer to each antenna which are then multiplied together in pairs to correct visibilities.

Atmospheric opacity is estimated for each baseband from fitting the 183 GHz water vapour line to the measurements by the WVRs. This requires that the antenna is connected to the correlator which is not the case for the PM antennas during single-dish observations. The online ALMA system then supplies the measurements from the nearest 12 m antenna

connected to the correlator. A typical range of τ for the ALMA site is below 0.05 for Band 3, and for Band 6 it varies in the range 0.04-0.15 (Figure 29).

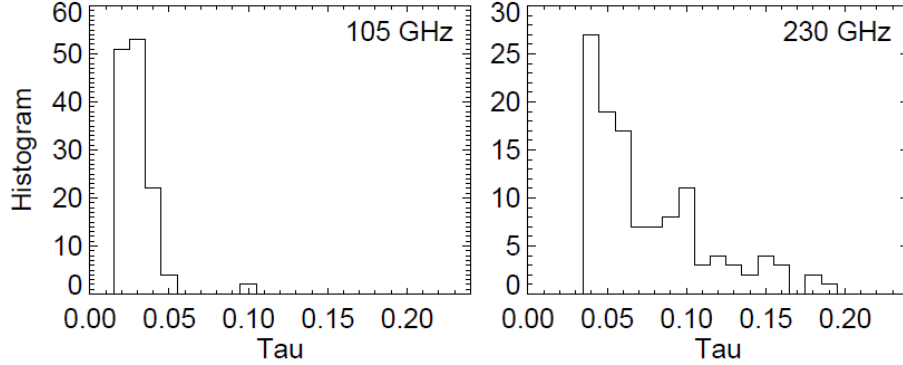


Figure 29: The distributions of daytime atmospheric opacity for Band 3 (left) and Band 6 (right), based on solar single-dish datasets. (White et al. 2017)

Since TELCAL and CASA currently do not implement the dual-calibration method discussed here, it is interesting to compare the calibration values computed by each method. A single load calibration method, where only the ambient temperature load is measured, gives the following equation for the source brightness temperature:

$$T_{src}^{single} = \frac{(P_{sky} - P_{zero})(P_{src} - P_{off})T_{amb}}{\eta_1 \eta_{fss} e^{-\tau} (P_{amb} - P_{sky})(P_{off} - P_{zero})} \quad (19)$$

A comparison of calibration calculation on a band 6 dataset for three different methods, dual-load, single-load and ALMA/CASA, is shown in Table 8. The values presented are averages of the middle section of each calibration scan with a standard deviation of 0.1%. Since solar emission is not linearly polarized, it is expected that all polarizations would give similar results. The same holds for the basebands since frequency difference is too small to account for real difference in brightness temperature coming from different layers in the solar atmosphere.

Table 8: A comparison of calibration data for a representative Band 6 dataset. Values are given for 4 basebands and two linear polarizations. Powers are median measurements in arbitrary units. The τ values are reported by the online system while T_{rec} and T_{sky} are calculated using expressions (14) and (15), respectively. Dual denotes temperature values computed using dual-load calibration method, single stands for single-load, while Atmcal denotes values from ALMA system/CASA calibration. (White et al. 2017)

	230 GHz		232 GHz		246 GHz		248 GHz	
	X	Y	X	Y	X	Y	X	Y
P_{hot}	0.629	0.560	0.579	0.565	0.586	0.494	0.593	0.517
$P_{ambient}$	0.590	0.534	0.545	0.539	0.553	0.472	0.560	0.493
P_{sky}	0.456	0.447	0.426	0.453	0.437	0.402	0.446	0.417
P_{off}	0.257	0.319	0.254	0.317	0.268	0.311	0.267	0.329
P_{zero}	0.002	-0.001	0.009	-0.003	0.007	-0.011	0.007	-0.038
τ	0.142	0.142	0.156	0.156	0.156	0.156	0.182	0.182
T_{rec} (K)	729	1058	754	1092	790	1195	807	1176
T_{sky} (K)	57.8	71.2	60.9	72.1	61.6	74.4	65.3	80.2
T_{sys}^{dual} (K)	955	1370	1003	1432	1048	1562	1101	1585
T_{sys}^{single} (K)	1191	1814	1268	1904	1329	2097	1420	2189
T_{Atmcal}^{sys} (K)	1019	1575	996	1478	1041	1621	1159	1826
Disk T_B^{dual} (K)	5955	5979	5963	5990	5876	5907	5889	5903
Disk T_B^{single} (K)	6124	6523	6128	6471	6056	6447	6012	6453
Disk T_B^{Atmcal} (K)	6507	7107	5907	6454	5874	6548	6226	7820

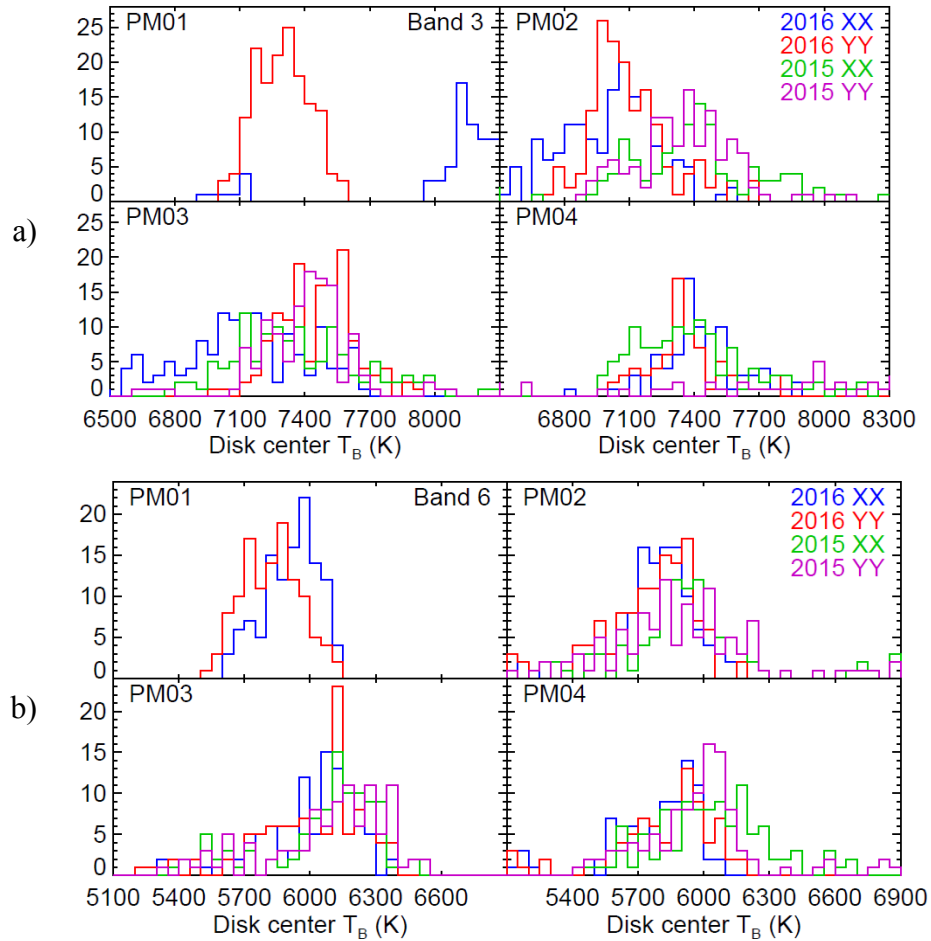


Figure 30: Distributions of the median brightness temperature obtained in a 120 x 120 (a) and 80 x 80 (b) arcsec region at disk center for Band 3 and Band 6 datasets from 2015 and 2016. The data are separated by antenna, year and polarization. There were no PM01 measurements in 2015. (White et al. 2017)

The brightness temperature obtained by using CASA processing, T^{Atmcal} , is corrected by the correction factor from Table 7. The variations in values seen in Table 8 are typical for a solar single-dish dataset. It is interesting to note that, despite the variations in measured values, dual-load calibration method gives consistent results across all basebands and polarizations, while the single-load and CASA methods vary much more and have systematically larger values for Y polarization compared to X polarization.

Applying the dual-load calibration method on more datasets from 2015 and 2016, it can be seen that it doesn't always produce such consistent results (Figure 30). There is dispersion in values of the order of several hundred kelvins. Moreover, many times different polarization products have systematically different values. In 2015, it is found that PM04 had troubles measuring Y polarization zero power whose values varied wildly in Band 3, while in 2016 PM01 and PM03 had troubles with X polarization in Band 6. The exact cause of this is not yet known. When these bad measurements are removed from the dataset and all PM antennas and polarizations are merged, brightness temperature distributions shown in Figure 31 are produced.

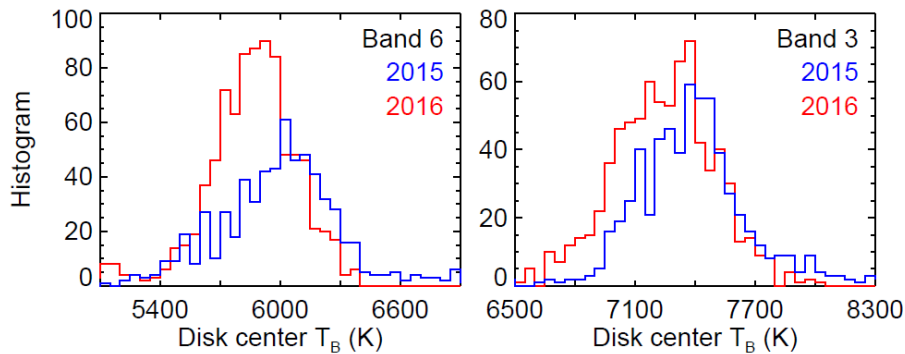


Figure 31: The distributions of the disk center brightness temperatures at Band 6 (left) and Band 3 (right) for all PM antennas merged. The distributions for measurements performed in 2015 (blue) and in 2016 (red) are plotted separately. (White et al. 2017)

Slightly smaller values of brightness temperature are observed in 2016 than in 2015. This may be due to the declining solar activity in that period but also it may be a result of an overall uncertainty in the calibration. Fitting Gaussian functions to the measured distributions gives values listed in Table 9. From these values, we deduce the mean quiet Sun level to be 7300 ± 200 K for Band 3 and 5900 ± 200 K for Band 6. Because of the uncertainty involved with the current CASA processing, it is recommended to scale the single-dish solar maps to these values.

Table 9: Mean brightness temperatures for datasets from 2015 and 2016. Mean values and standard errors were obtained by fitting Gaussians to the measured distribution. (White et al. 2017)

	Band 3	Band 6
2015	7390 ± 220 K	6040 ± 250 K
2016	7280 ± 250 K	5900 ± 190 K

It is interesting to compare these values to the previous measurements in the millimeter wavelength range. Loukitcheva et al. (2015) give a compilation of measurements which is shown in Figure 32. ALMA measurements are in agreement with other results, but it should

be noted that the comparison is not straightforward because of the differences in spatial resolution of different instruments.

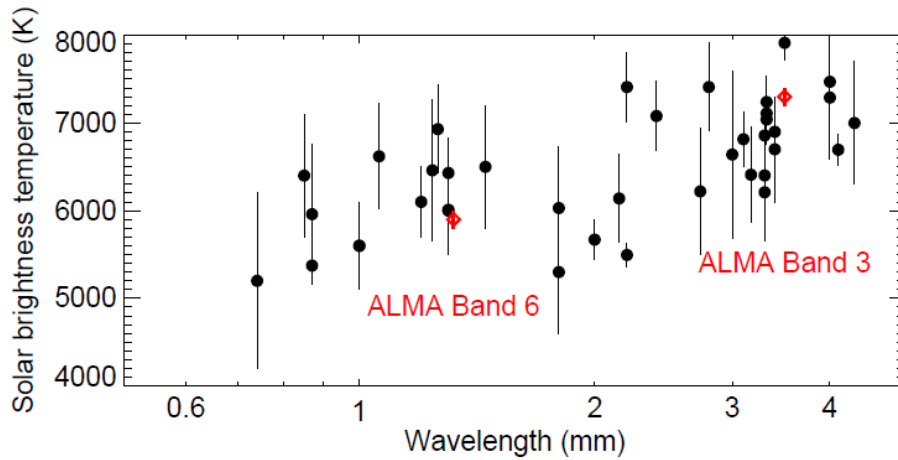


Figure 32: Recommended ALMA values of the quiet Sun level on the disk center compared to previous measurements collected by Loukitcheva et al. (2015). (White et al. 2017)

4.3 Examples of Single-dish Images

Representative examples of ALMA fast-scanning images of the Sun from December 17, 2015 are shown in Figure 33. These images are generated using CASA tasks implementing calibration and gridding as described earlier. The brightness temperature display range is chosen to show the full range of brightness temperatures on the disk at Band 6 (left) and Band 3 (right), and lower-level contours are plotted to show off-limb features. For comparison, we show a 30.4 nm image and a line-of-sight magnetogram from instruments on the Solar Dynamics Observatory (SDO). The 30.4 nm image is dominated by the He II line and represents the upper chromosphere. As expected, the bright regions in the ALMA images match the bright regions at 30.4 nm and the areas of strong magnetic field where additional atmospheric heating would be expected. However, there are obvious differences in the relative brightness of different features: e.g., the brightest feature in the south-east quadrant in the ALMA images is not the brightest feature in the same area in the 30.4 nm image. Further, there are significant differences in the relative brightness of individual features at 230 and 93 GHz, e.g., at the same resolution, the active region plage east of the large sunspot is relatively brighter at 230 GHz than at 93 GHz. Prominences visible above the limb in the ALMA images match off-limb emission in the 30.4 nm image, although again with differences in relative brightness. A large sunspot is present in the north-east quadrant, coincident with the intense negative polarity in the magnetogram. It is clearly visible as a depression surrounded by a bright rim in the 230 GHz image, but is less obvious at the 60 arcsec resolution of the 93 GHz image. Large-scale cool features are present over filament channels at both ALMA frequencies.

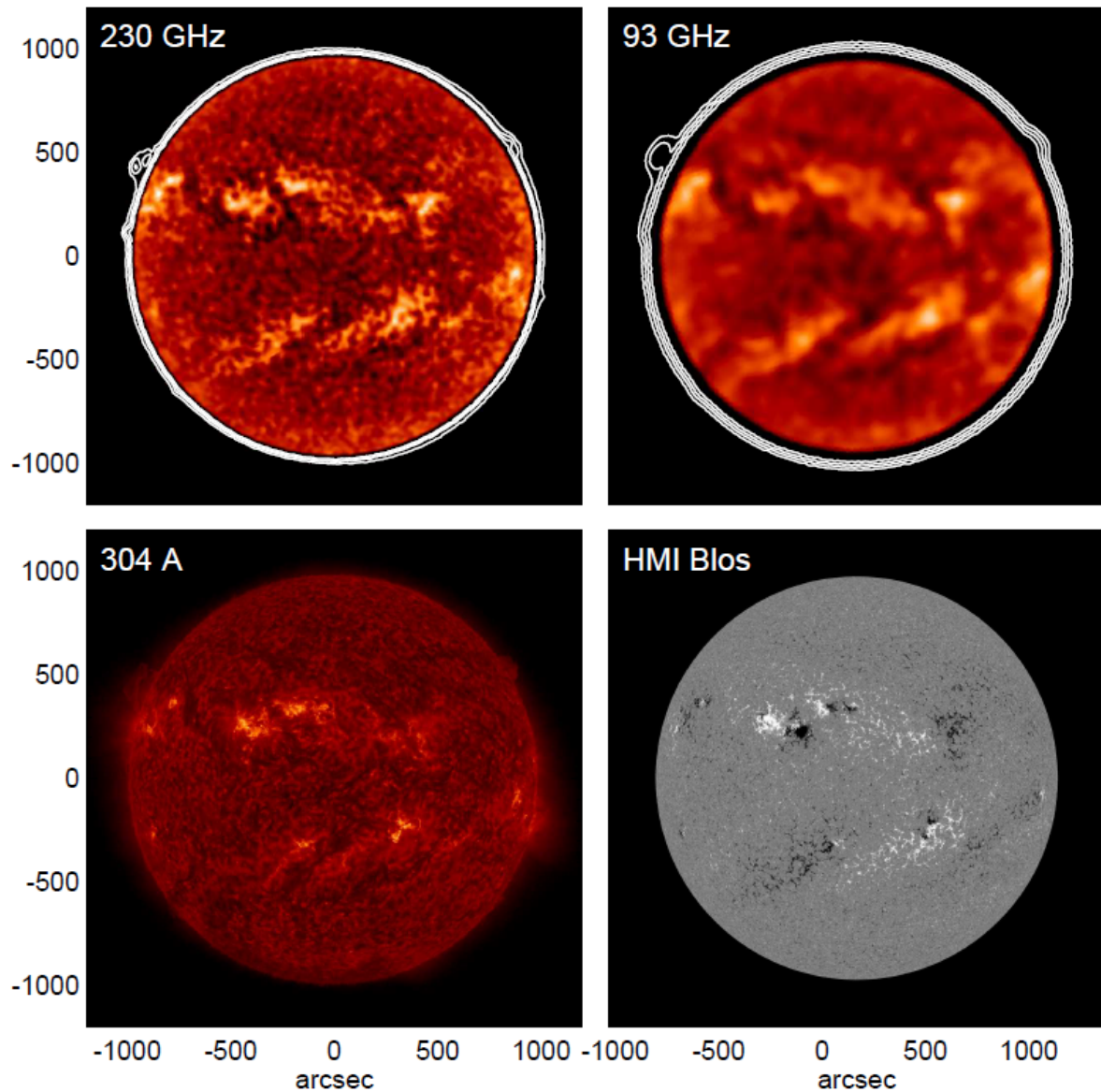


Figure 33: ALMA fast-scanning observations of the Sun on 2015 December 17 at Band 6 (230 GHz at 14:33 UT, upper left panel) and Band 3 (93 GHz at 18:15 UT, upper right panel). In order to emphasize structure on the disk, the 230 GHz image color display ranges from 5300 to 7400 K, while the 93 GHz color display ranges from 6700 to 8800 K. Low-level contours are plotted at 300, 600, 1200, and 2400 K in order to show features above the limb. For comparison, we show SDO/AIA image of the Sun at 30.4 nm (lower left panel, dominated by the He II line from the upper chromosphere (at 14:44 UT to match 230 GHz), and a line-of-sight magnetogram from the Helioseismic and Magnetic Imager (HMI) on SDO at 18:30 UT (lower right panel). (White et al. 2017)

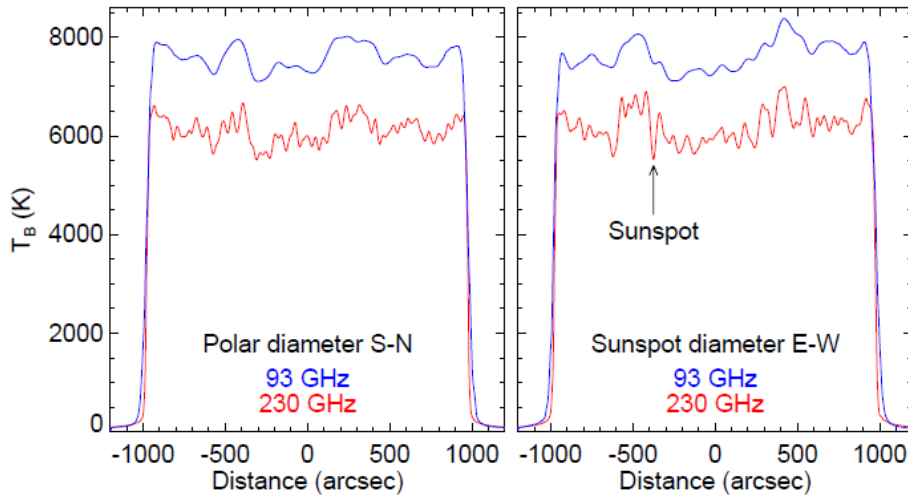


Figure 34: Profiles across the solar disk at 93 (blue) and 230 GHz (red) at two angles: from the south pole to the north pole at apparent disk center, and on a diameter through the large sunspot (azimuth 63.8° east of north), from east to west. The 93 GHz image has been rotated back to the time of the 230 GHz image for comparison. The location of the sunspot in the right panel is marked by an arrow. (White et al. 2017)

To provide a more quantitative picture of the level of variability across the disk, Figure 34 shows profiles through disk center from both ALMA images along two angles: a polar cut from south to north (left panel), and a diameter at 64° east of north that passes through the large sunspot (right panel). A direct comparison between the 93 and 230 GHz profiles is not possible due to the differing resolutions at the two frequencies: the larger beam at 93 GHz is averaging over about 6 resolution elements at 230 GHz. The polar cut is dominated by quiet-Sun fluctuations amounting to a few hundred K on small spatial scales. The sunspot diameter crosses a number of bright regions, and in particular the active region encompassing the sunspot, between about -700 and -300 arcsec, which is around 1000 K brighter than the adjacent regions at 230 GHz. The dip in emission over the sunspot umbra is clearly visible in the 230 GHz profile, being less obvious at the resolution of the 93 GHz data.

In Figure 35, single-dish fast-scan image of the Sun is compared to SDO/AIA 19.3 nm channel (adapted from Brajša et al., 2017a). Small bright regions in ALMA image (marked with blue rectangles) correspond to coronal bright points in AIA image. A zoomed-in region of ALMA image just below the sunspot (visible as a dark point inside bright area) is compared with the SDO/HMI magnetogram in the lower panel. Magnetic bipoles are found at locations of ALMA bright points.

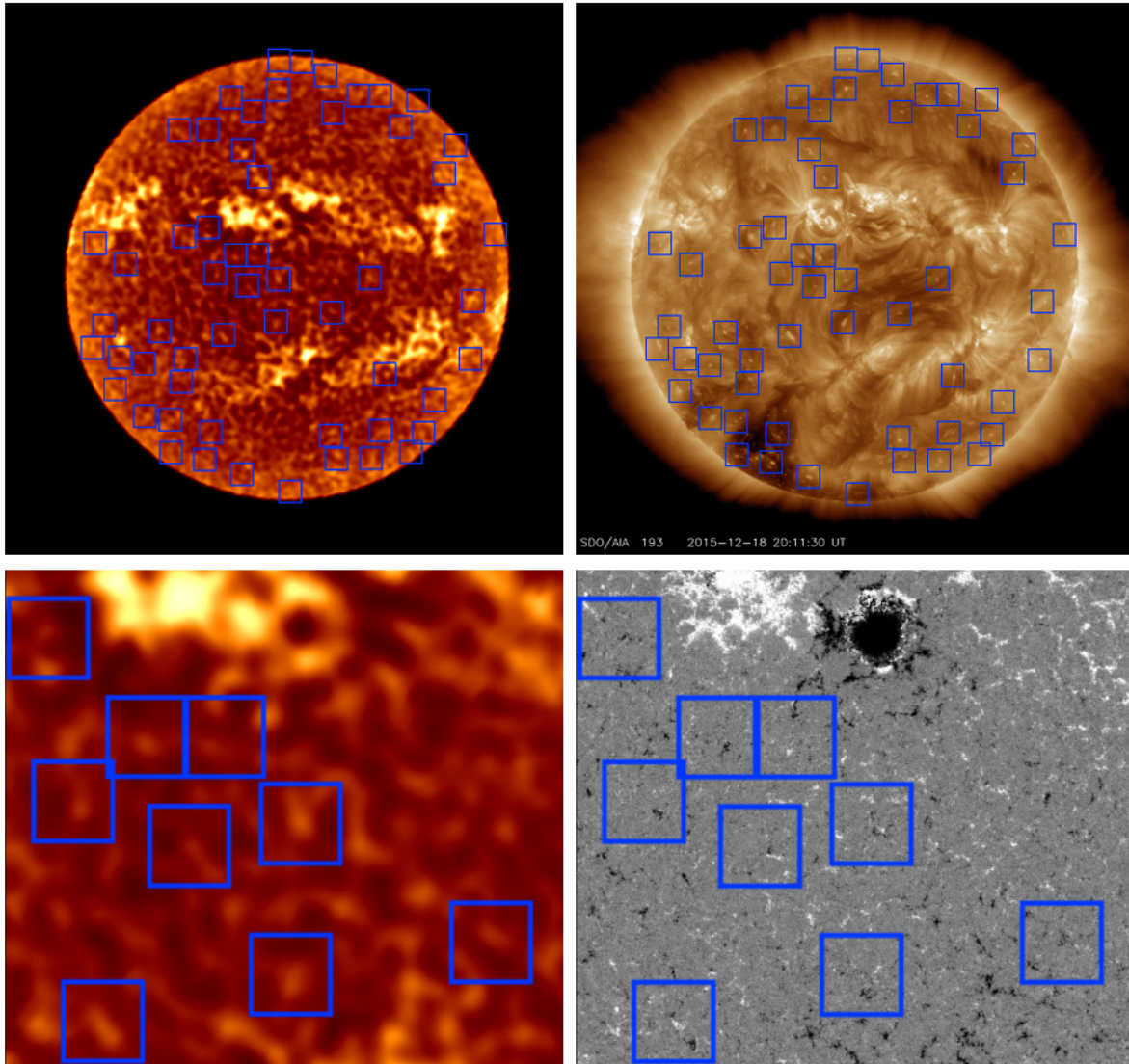


Figure 35: ALMA single-dish fast scan image of the Sun in Band 6 (upper left) compared to the SDO/AIA 19.3 nm channel. Small bright regions in ALMA image (marked by blue rectangles) correspond to coronal bright points in AIA image. A zoomed-in region of ALMA image is compared to SDO/HMI magnetogram in the lower panel. Magnetic bipoles are found at the locations of bright points. (Brajša et al. 2017a)

During the 2015 commissioning campaign, single-dish fast scanning tests were performed also in Band 9. Figure 36 shows a one Band 9 solar image obtained using the double-circle pattern. This image shows a striking network pattern in addition to bright active regions with fine resolution enabled by the small size of Band 9 beam. It is interesting to note that for Band 9, mixer detuning is not used since atmospheric attenuation is significant. Moreover, opacity variations also become a problem and this image shows how double-circle pattern is capable to overcome it by repeatedly scanning the central region.



Figure 36: Full-disk image of the Sun in Band 9 obtained with double-circle fast-scanning during December 2015 solar campaign. Fine structure is seen in this image down to the nominal beam size of 9 arcsec. The contrast represents brightness temperature structure in the solar chromosphere: the network/cell pattern visible across much of the disk is due to convection cells, while active regions are bright.

5 SOFTWARE REQUIREMENTS FOR SOLAR OBSERVING

5.1 ALMA Observing Tool

The ALMA Observing Tool (OT) is a software tool used for proposal preparation and submission, as well as for generation and tweaking of scheduling blocks (SBs) after the proposal has been accepted.

Specifics of the solar observing modes impose certain constraints on the OT for solar proposals. From the Cycle 4 ObsMode summary report, solar observing is considered a “non-standard” observing mode since it requires detuning of SIS mixers and use of the hybrid arrays and simultaneous TP observing. Also, solar images still have to be manually calibrated and cannot be passed through the calibration/imaging pipeline software. The following inputs to the OT were requested and implemented for Solar observing starting in Cycle 4. For Cycle 5, the only change was in new integration limit of 1 second which does not affect the OT GUI.

OT Requirements

- Proposal type: regular
- Scientific category: Stellar Evolution and the Sun
- Keywords: The Sun
- Field setup: Source should be set to Solar System object – Sun. This will indicate that the rest of the science goal (SG) should be treated as solar observing. Choice of "Sun" should behave like "ephemeris" – an external ephemeris file is required. This file can be generated using the ALMA Solar Ephemeris Generator Tool. Individual pointing(s) or rectangular field should both be available. Expected source properties would only offer "Active" or "Quiet" Sun, corresponding to MD2 and MD1 modes.
- Spectral setup: in Cycle 4, only continuum band 3 and 6 with predefined frequencies and dual polarization should be available.
- Calibration setup: no change.
- Control and Performance: Solar observations will trigger a special array incorporating both 12-m and 7-m elements (both run through the BLC) to ensure adequate sampling of short spacings. In addition, TP fast scanning should be used simultaneously in the double circle pattern. The TP antennas should not be counted in the final number of 12-m antennas. The “Desired Sensitivity” field should be greyed out. The PI should only enter desired angular resolution (which will automatically select the appropriate antenna configuration) and enter the time required for the execution of a SB.
- Technical Justification: Solar observations only have to justify the angular resolution selection and integration time.

5.2 Coordinate Conversions for Solar Observing

The highly dynamic solar atmosphere makes it difficult to predict the appearance and position of interesting features like sunspots, filaments or flares. Differential rotation, meridional and proper motions all affect the position of solar objects. For example, a sunspot at the solar disk center will move by almost $220 \text{ arcsec day}^{-1}$, assuming only Carrington rotation. While it is possible to include the mean rotation profile for the position prediction, proper motions are

impossible to predict. With a realistic proper motion (including morphological changes) of 100 m s^{-1} , the sunspot will move another $11 \text{ arcsec day}^{-1}$, readily comparable with the field of view of $\sim 26 \text{ arcsec}$ in Band 6.

Solar physicists are accustomed to work in a solar coordinate frame, most usually helioprojective or heliographic, while ALMA OT uses celestial coordinate system (ICRF). Therefore, it is necessary to have a tool for easy selection of solar features which will generate an ephemeris file compatible with the OT, taking into account differential rotation and other effects. For this purpose, ALMA Solar Ephemeris Generator Tool⁴ was developed.

The problem of converting of the coordinates can be put this way: given equatorial coordinates of the target (specified as right ascension, α , and declination, δ), the equatorial coordinates of the solar center (α_0 , δ_0) and the position angle of the solar north pole (P angle, measured from celestial north towards east), the aim is to find the helioprojective coordinates (θ_x , θ_y , sometimes also called solar x , y) of the target. Also for the reverse problem, if (x, y) are given, to find the target (α, δ) .

Approximate method

Since the Sun is only ~ 0.5 degrees in diameter when viewed from Earth, it is possible to consider the small angle approximation and planar geometry for targets near the Sun. In that case, the conversion between equatorial and helioprojective coordinates is just a rotation of the differences of equatorial coordinates of the Sun and the target by the solar P angle, corrected for the R.A. shrinkage with declination ($\cos \delta_0$ term):

$$\theta_x = -(\alpha - \alpha_0) \cos \delta_0 \cos P - (\delta - \delta_0) \sin P \quad (20)$$

$$\theta_y = (\alpha - \alpha_0) \cos \delta_0 \sin P + (\delta - \delta_0) \cos P \quad (21)$$

Helioprojective coordinates (θ_x , θ_y) are usually measured in arcseconds (positive towards solar west and north, hence the minus sign). Converting back to equatorial coordinates is straightforward:

$$\alpha = \frac{-\theta_x \cos P + \theta_y \sin P}{\cos \delta_0} + \alpha_0 \quad (22)$$

$$\delta = \theta_x \sin P + \theta_y \cos P + \delta_0 \quad (23)$$

This method should work for small angular distances from the solar center, say up to 10 arcmin. Numerical tests show that error of 1 arcsec is expected for targets on the solar limb. It starts to fail badly at angular distances larger than 1 degree and around poles, so a better method is needed.

Exact method

By using spherical geometry it is possible to derive exact equations for the transformation (Figure 37):

⁴ <http://celestialscenes.com/alma/coords/CoordTool.html>

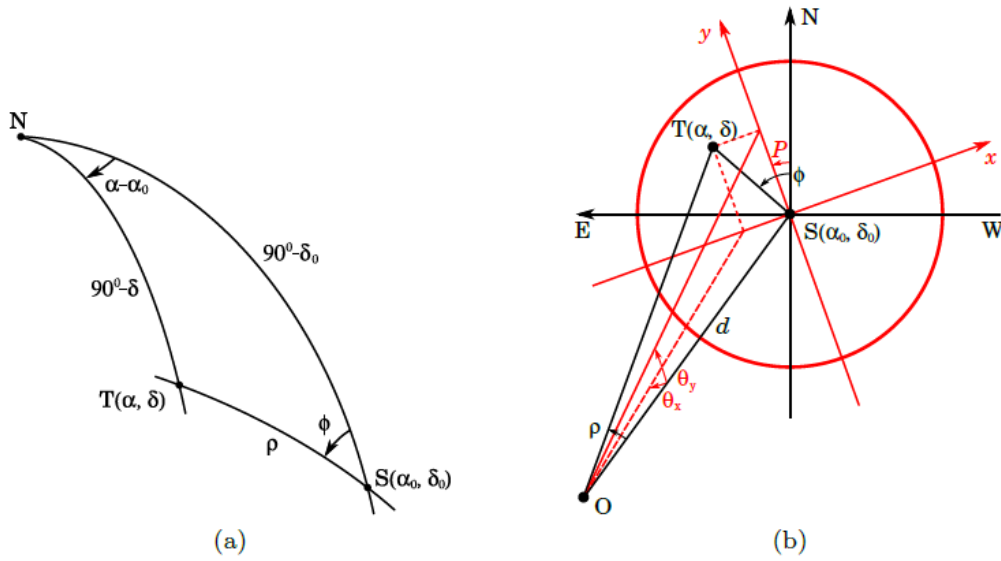


Figure 37: a) A spherical triangle on the celestial sphere defined by the Sun center (S), target (T) and celestial north (N). b) Target (T) located on the solar disc (red circle) with helioprojective coordinate system (in red) and equatorial coordinate system (black). Observer (O) is located at a distance d from the Sun.

$$\cos \rho = \cos \delta \cos \delta_0 \cos(\alpha - \alpha_0) + \sin \delta \sin \delta_0 \quad (24)$$

$$\tan \phi = \frac{\sin(\alpha - \alpha_0)}{\tan \delta \cos \delta_0 - \sin \delta_0 \cos(\alpha - \alpha_0)} \quad (25)$$

$$\tan \theta_x = -\tan \rho \sin(\phi - P) \quad (26)$$

$$\tan \theta_y = \tan \rho \cos(\phi - P) \quad (27)$$

Reverse equations are:

$$\tan(\phi - P) = -\frac{\tan \theta_x}{\tan \theta_y} \quad (28)$$

$$\tan \rho = -\frac{\tan \theta_x}{\tan \theta_y} \quad (29)$$

$$\sin \delta = \sin \delta_0 \cos \rho + \cos \delta_0 \sin \rho \cos \phi \quad (30)$$

$$\tan(\alpha - \alpha_0) = \frac{\sin \rho \sin \phi}{\cos \rho \cos \delta_0 - \sin \rho \sin \delta_0 \cos \phi} \quad (31)$$

These equations are exact. However, because computers have limited precision (rounding errors), numerical problems can arise. The equation for angular distance in (24) has problems

for small distances because cosine term changes slowly and is very close to one. Another expression can be used instead, which takes into account most problems but still has rounding errors for special antipodal points:

$$\sin \frac{\rho}{2} = \sqrt{\sin^2 \frac{\delta - \delta_0}{2} + \cos \delta \cos \delta_0 \sin^2 \frac{\alpha - \alpha_0}{2}} \quad (32)$$

Probably the best way is to use the equation for the ellipsoid by Vincenty (1975), adapted to circle by setting equal axes:

$$\tan \rho = \frac{\sqrt{[\cos \delta \sin(\alpha - \alpha_0)]^2 + [\cos \delta_0 \sin \delta - \sin \delta_0 \cos \delta \cos(\alpha - \alpha_0)]^2}}{\sin \delta \sin \delta_0 + \cos \delta \cos \delta_0 \cos(\alpha - \alpha_0)} \quad (33)$$

Although more complicated, this one should be numerically stable for all angles and distances.

5.3 ALMA Solar Ephemeris Generator Tool

The tool was developed by the Czech ARC Node to be used together with the OT in preparing solar observations and was tested during the December 2015 solar campaign. It is a javascript based application which runs in any modern browser and on many different operating systems. The source and documentation can be found in SCIREQ-930 ticket and also on the hosting web site⁵.

User interface consists of several panels (Figure 38). In the input panel, it is possible to select the latest SDO/AIA image in several bands or to upload users own FITS file. Currently, only uncompressed FITS with defined solar WCS keywords using CROTA2 formalism are supported. Visualization and display panels enable user to pan and zoom in/out the region of interest or to show/hide coordinate grids and tweak the image display by false coloring and level scaling functions typical of other astronomical software packages and the OT.

The actual pointing is done by clicking the desired feature with a green cross marking the position. The coordinates of the pointing are displayed in several coordinate systems inside the pointing panel, where it is also possible to manually define the pointing.

Finally, in the observation panel, the user defines start and end times of the observation and differential rotation profile which will be used for generation of an OT-compatible ephemeris file. There are several rotation profiles to choose from or the user can define his/her own. Clicking "Generate ephemeris file for OT" will display the generated file which can be downloaded by following "Download data below" link and then imported into the OT.

The ephemeris file is generated from the JPL Horizons file which the tool queries directly from Horizons website. However, during Cycle 4 regular observing sessions there was a period when JPL Horizons site went offline and hence the Ephemeris Tool was unable to function properly. Work is currently underway to enable precise ephemeris calculations in the Ephemeris Tool even when JPL site goes down.

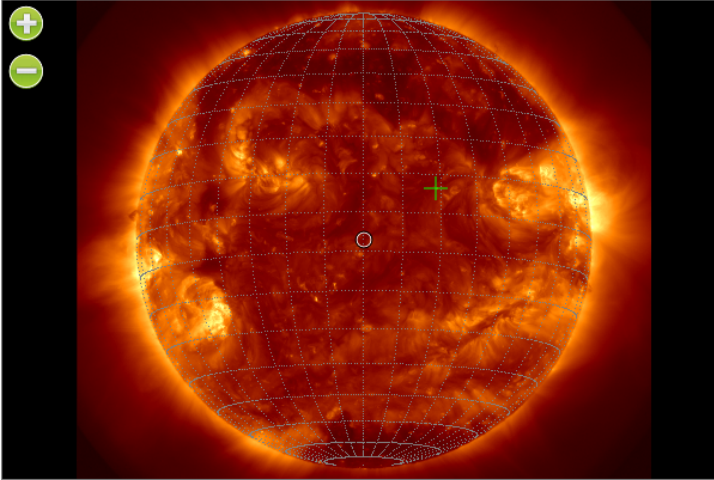
⁵ <http://celestialscenes.com/alma/coords/CoordTool.html>

Input FITS file

File: AIA synoptic 193 (latest) No file selected.
 Date: 2016-02-23T21:52:41.84 Size: 1024 x 1024 Format: 32

Visualization

Scaling function: cuberoot Color: heat Frame < 0 > of 1.
 Show grid Stonyhurst
 Show ALMA 12m beam size in band: Band 3
 cursor (wcs) = (441.52,-285.52), intensity = 646.9375



Pointing

pixel (x, y)	642.13	603.73	
helioprojective (x, y)	313.52	221.36	arcsec
heliographic (CMD, B)	18.893	6.405	degrees
heliographic (L, B)	303.356	6.405	degrees

Observation

Start of observation (UT): 2016-02-23T21:58:08
 End of observation (UT): 2016-02-24T21:58:08
 Step size (minutes): 20
 Differential rotation profile: H-alpha filaments (Brajša et al., 1991)
 A: 14.45 B: -0.11 C: -3.69
 Height above photosphere (km): 40000

Download Data Below

```

*****
Revised : Jul 31, 2013                               Sun
PHYSICAL PROPERTIES (revised Jan 16, 2014):
GM (10^11 km^3/s^2) = 1.3271244004193938  Mass (10^30 kg) ~ 1.998
Radius (photosphere) = 6.963(10^5) km  Angular diam at 1 AU = 1915
Solar Radius (IAU) = 6.955(10^5) km  Mean density = 1.408
Surface gravity = 274.0 m/s^2  Moment of inertia = 0.083
Escape velocity = 617.7 km/s  Adopted sidereal per = 25.38
Pole (RA,DEC in deg.) = 286.13,63.87  Obliquity to ecliptic = 7 de
Solar constant (1 AU) = 1367.6 W/m^2  Solar lumin. (erg/s) = 3.828
Mass-energy conv rate = 4.3(10^12 gm/s)  Effective temp (K) = 5778
Surf. temp (photosphr) = 6600 K (bottom)  Surf. temp (photosphr) = 4400
Photospheric depth = ~400 km  Chromospheric depth = ~2500
Sunspot cycle = 11.4 yr  Cycle 22 sunspot min. = 1999
Motn. rel to nrby str= apex : RA=271 deg; DEC=+30 deg
                        speed: 19.4 km/s = 0.0112 AU/day
  
```

Figure 38: User interface of the Solar Ephemeris Tool

The Ephemeris Tool comes with a user manual and it is served on several sites for backup purposes. Currently, there are no plans to include the tool functionality into the OT.

5.4 The Common Astronomy Software Applications (CASA) Package

CASA package is the standard software used to reduce, image and analyze ALMA data. As has been shown in previous chapters, the CASA version 4.7 or later works well with solar data although there are several considerations to note. For reduction of solar data, an Analysis Utilities CASA add-on package is needed because of the specific solar amplitude calibration method. Other than that, a standard calibration method for ALMA data can be used. Imaging of single-dish data works well, although a correction factor is needed to account for different calibration schemes used by CASA/ALMA TELCAL and single-dish solar observing. A progress is underway to implement the solar calibration scheme.

Reduction and imaging of interferometric solar data, both single pointing and mosaic, works well even though the Sun is such a difficult target. Mosaic images need recalculation of pointing coordinates to the center of the field of view with a "fixplanets" task due to the movement of the Sun relative to the celestial coordinate frame during observing. To improve the image quality, it is possible to use all four spectral windows. Minor imaging artifacts can be seen in images, but comparisons with solar images of the same region of the solar atmosphere from other observatories confirm that most of the features detected have similarly-shaped counterparts. Better imaging is obtained with natural weighting of longer baselines. Other imaging methods, such as maximum entropy method have not been tried but are expected to provide even better images.

Combining of total power single-dish data with interferometric data through feathering also seem to work although the brightness temperatures in the resulting image are a few percent larger than in the related single-dish image. The reason for this is as yet unknown.

What is also missing in CASA is support for solar coordinate systems. While this would be a nice feature, it is not essential because ready-made scripts can be used to convert images. One such script has been developed in Python/SunPy and is being adapted to CASA.

5.4.1 Coordinate System Support for Solar Images in CASA

B. Chen proposed that CASA should produce, for the solar case, standard FITS image files with coordinates familiar to the solar community and compatible with other tools (IDL, SolarSoft, SunPy, etc.). The coordinate system proposed is helioprojective Cartesian with gnomonic (TAN) projection. In this coordinate system, X and Y axes point to solar west and solar north. The units are described in angle:

$$\theta_x = x/d \cdot \pi/180 \cdot 3600, \quad \theta_y = y/d \cdot \pi/180 \cdot 3600 \quad (34)$$

where d is the distance between the observer and the Sun center. FITS tags should be constructed in a way that is compatible with the World Coordinate System (WCS; Thompson, 2006).

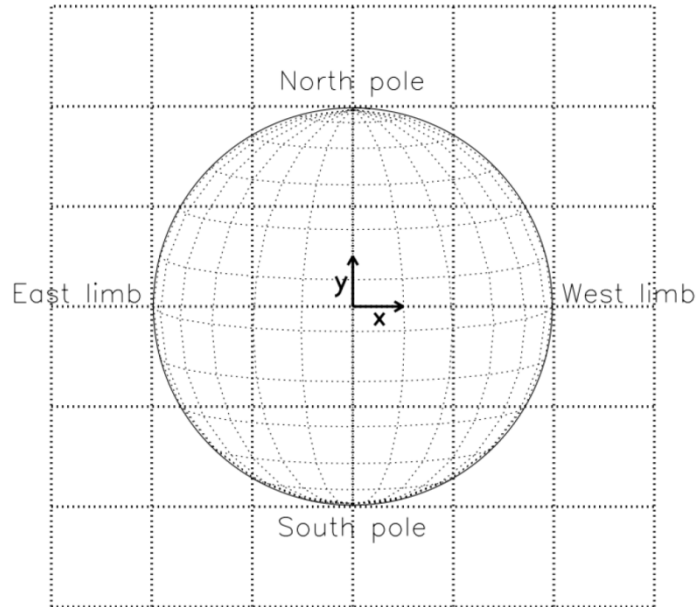


Figure 39: Heliographic and helioprojective coordinate systems.

For this purpose, the following information is needed:

- Pointing coordinates at any given time in topocentric right ascension and declination (RA and DEC)
- Topocentric coordinates of the solar disk center, solar P angle, and sun-observer distance as a function of time, queried from JPL Horizons
- Information of the image: time, phase center, frequency (and bandwidth), polarization, clean beam

The following procedure is recommended:

1. Convert image center from celestial to helioprojective coordinates.
2. Rotate the image according to the solar P angle
3. Record the time of the image, say, integrated from t_1 to t_2 . Use the middle of the integration time $t_{\text{ref}} = (t_1 + t_2)/2$ as the reference time for image registration. Use the same time as a reference time for image synthesis.
4. Update FITS keywords of the rotated image:

```

CRVAL1 =  $\theta_x(t_{\text{ref}})$ 
CRVAL2 =  $\theta_y(t_{\text{ref}})$ 
CUNIT1 = 'arcsec'
CUNIT2 = 'arcsec'
CTYPE1 = 'HPLN-TAN'
CTYPE2 = 'HPLT-TAN'
DATE-OBS =  $t_1$ 
EXPTIME =  $t_2 - t_1$ 
DSUN_OBS = Sun-observer distance in meters

```

The following CASA tasks requested to provide such support:

- **“exportfits”**: with an option added to allow conversion to solar coordinates using the procedure as described above. Task parameters might be incorporated to query JPL Horizons for solar disk center position or import user supplied target coordinates.

- “viewer” or “imview”: add options to display solar FITS images in helioprojective Cartesian coordinates.

Sample FITS keywords are listed in Table 10.

Table 10: Sample FITS keywords for solar observing.

Keyword	Type	Value	Comment
#Note: Axes info			
NAXIS	LONG	4	/4D image: 2 spatial, 1 frequency, 1 polarization
NAXIS1	LONG	256	/Number of pixels in Solar X
NAXIS2	LONG	256	/Number of pixels in Solar Y
NAXIS3	LONG	10	/Number of frequency channels
NAXIS4	LONG	1	/Number of polarization products
#Note: This is for a single clean beam. Probably needs some way to store the information for variable beams			
BMAJ	DOUBLE	0.01000000	/Major axis of the clean beam, in degrees
BMIN	DOUBLE	0.00600000	/Minor axis of the clean beam, in degrees
BPA	DOUBLE	-175.00000	/Position angle of the clean beam, in degrees
BTYPE	STRING	'Intensity'	/Type of the image values
BUNIT	STRING	'Jy/beam'	/Image pixel units (K, Jy/beam, etc)
#Note: General info			
DATEOBS	STRING	'2014-12-12T19:00:00.000'	/Start time of the integration
EXPTIME	DOUBLE	60.0000000	/Integration time of the image, in seconds
CTYPE1	STRING	'HPLN-TAN'	/X axis label (theta_X)
CRVAL1	DOUBLE	0.0000000	/X coordinate of the reference pixel
CDELTA1	DOUBLE	4.000000	/Image plate scale in X, in arcsecs
CRPIX1	DOUBLE	129.00000	/reference pixel in X
CUNIT1	STRING	'arcsec '	/X axis unit
CTYPE2	STRING	'HPLT-TAN'	/Y axis label (theta_Y)
CRVAL2	DOUBLE	0.0000000	/Y coordinate of the reference pixel
CDELTA2	DOUBLE	4.0000000	/Image plate scale in Y, in arcsecs
CRPIX2	DOUBLE	129.00000	/reference pixel in Y
CUNIT2	STRING	'arcsec '	/Y axis unit
CTYPE3	STRING	'FREQ'	/Frequency axis (3 rd axis)
CRVAL3	DOUBLE	100.0000e+09	/Coordinate of the ref. pixel in the frequency axis
CDELTA3	DOUBLE	1.00000e+09	/Frequency channel width
CRPIX3	DOUBLE	1.0000000	/Reference pixel in the frequency axis
CUNIT3	STRING	'Hz'	/Frequency axis unit
CTYPE4	STRING	'STOKES'	/4 th axis, Stokes
CRVAL4	DOUBLE	1.0000000	/Coordinate of the reference pixel in the Stokes axis
CDELTA4	DOUBLE	1.0000000	/
CRPIX4	DOUBLE	1.0000000	/Reference pixel in the Stokes axis
CUNIT4	STRING	"	
PC1_1	DOUBLE	1.0000000	/Rotation angle=0
PC2_2	DOUBLE	1.0000000	
PC3_3	DOUBLE	1.0000000	
PC4_4	DOUBLE	1.0000000	
#Note: information about the target			
OBJECT	STRING	'SUN'	/Observing object
DSUN_OBS	DOUBLE	1.4960E+11	/Distance from the Sun to the observer, in meters
HGLN_OBS	DOUBLE	0.0	/Stonyhurst heliographic longitude of the observer, in degrees
HGLT_OBS	DOUBLE	0.0	/Stonyhurst heliographic latitude of the observer, in degrees

6 REFERENCES

- Brajša, R., Kuhar, M., Benz, A. O., Skokić, I., Sudar, D., Wedemeyer, S., Barta, M., De Pontieu, B., Kim, S., Kobelski, A., Shimojo, M., White, S., Yagoubov, P., Yan, Y.: 2017a, A comparison of solar ALMA observations and model based predictions of the brightness temperature, *Astronomy and Astrophysics*, submitted.
- Brajša, R., Skokić, I., Sudar, D., Benz, A. O.: 2017b, Identification of structures in ALMA solar interferometric images, *Astronomy and Astrophysics*, to be submitted.
- Brogan, C. L. and Hunter, T. R.: 2014, ALMA Single-dish Imaging Parameters, *NAASC Memo 114*.
- Hills, R. E.: 2015, Choice of Frequencies for Solar Observing, *ALMA Report CSV-3162*.
- Hills, R. E.: 2016, PM Antenna Servo Characterization, *ALMA CSV-3243 Report*.
- Iwai, K.: 2016, Fast Scan Pattern Simulation, *ALMA CSV-3244 Report*.
- Iwai, K.: 2016a, Nonlinearity of ALMA Antennas in Detuning Mode 1, *ALMA Report CSV-3246*.
- Loukitcheva, M., Solanki, S. K., Carlsson, M. and White, S.M.: 2015, Millimeter radiation from a 3D model of the solar atmosphere. I. Diagnosing chromospheric thermal structure, *Astronomy and Astrophysics*, 575, A15.
- Shimojo, M., Bastian, T. S., Hales, A. S., White, S. M., Iwai, K., Hills, R. E., Hirota, A., Phillips, N. M., Sawada, T., Yagoubov, P., Siringo, G., Asayama, S., Sugimoto, M., Brajša, R., Skokić, I., Barta, M., Kim, S., de Gregorio, I., Corder, S. A., Hudson, H. S., Wedemeyer, S., Gary, D. E., De Pontieu, B., Loukicheva, M., Fleishman, G. D., Chen, B., Kobelski, A., Yan, Y.: 2017, Observing the Sun with ALMA: High Resolution Interferometric Imaging, *Solar Physics*, in press.
- Tamura, Y. and Sugimoto, M.: 2012, Preliminary Analysis of the Forward Efficiency, *ALMA SV Report SYS #132*.
- Thompson, W. T.: 2006, Coordinate systems for solar image data, *Astronomy and Astrophysics*, 449, 791
- Vincenty, T.: 1975, Direct and Inverse Solutions of Geodesics on the Ellipsoid with application of nested equations, *Survey Review*. XXIII (176): 88–93.
- Wedemeyer, S., Bastian, T., Brajša, R., Hudson, H., Fleishman, G., Loukitcheva, M., Fleck, B., Kontar, E. P., De Pontieu, B., Yagoubov, P., Tiwari, S. K., Soler, R., Black, J. H., Antolin, P., Scullion, E., Gunár, S., Labrosse, N., Ludwig, H.-G., Benz, A. O., White, S. M., Hauschildt, P., Doyle, J. G., Nakariakov, V. M., Ayres, T., Heinzl, P., Karlicky, M., Van Doorselaere, T., Gary, D., Alissandrakis, C. E., Nindos, A., Solanki, S. K., Rouppe van der Voort, L., Shimojo, M., Kato, Y., Zaqarashvili, T., Perez, E., Selhorst, C. L., Barta, M.: 2016, Solar Science with the Atacama Large Millimeter/Submillimeter Array—A New View of Our Sun, *Space Science Reviews*, Volume 200, Issue 1-4, pp. 1-73

White, S. M., Iwai, K., Phillips, N. M., Hills, R. E., Hirota, A., Yagoubov, P., Siringo, G., Shimojo, M., Bastian, T. S., Hales, A. S., Sawada, T., Asayama, S., Sugimoto, M., Marson, R. G., Kawasaki, W., Muller, E., Nakazato, T., Sugimoto, K., Brajša, R., Skokić, I., Barta, M., Kim, S., Remijan, A. J., de Gregorio, I., Corder, S. A., Hudson, H. S., Loukitcheva, M., Chen, B., De Pontieu, B., Fleishmann, G. D., Gary, D. E., Kobelski, A., Wedemeyer, S., Yan, Y.: 2017, Observing the Sun with ALMA: Fast-scan Single-dish Mapping, *Solar Physics*, in press.

Yagoubov, P.: 2016, Recommendations on mixer de-tuning for Solar observations with ALMA, *ALMA CSV-3245 Report*.

Yagoubov, P.: 2013, Solar observations with ALMA - How to minimize saturation in SIS mixers, *IEEE*, 1.